ROBUST NUCLEI SEGMENTATION IN CYTOHISTOPATHOLOGICAL IMAGES USING STATISTICAL LEVEL SET APPROACH WITH TOPOLOGY PRESERVING CONSTRAINT

Shaghayegh Taheri Hosseinabadi

A thesis

in

The Department

of

Computer Science

Presented in Partial Fulfillment of the Requirements

For the Degree of Master of Computer Science

Concordia University

Montréal, Québec, Canada

April 2016

Concordia University

School of Graduate Studies

This is to certify that the thesis prepared

By: **Shaghayegh Taheri Hosseinabadi**

Entitled: **Robust Nuclei Segmentation in Cytohistopathological Images Using**

             Statistical Level Set Approach with Topology Preserving Constraint

and submitted in partial fulfillment of the requirements for the degree of

Master of Computer Science

complies with the regulations of this University and meets the accepted standards with respect

to originality and quality.

Signed by the final examining commitee:

Dr. G. Butler	Chair
Dr. A. Krzyzak	Examiner
Dr. C. Poullis	Examiner
Dr. T. D. Bui	Supervisor
Dr. T. Fevens	Supervisor

Approved by _____

Chair of Department or Graduate Program Director

_____

Dean of the Faculty of Engineering and Computer Science

Date _____

Abstract

Robust Nuclei Segmentation in Cytohistopathological Images Using Statistical
Level Set Approach with Topology Preserving Constraint

Shaghayegh Taheri Hosseinabadi

Computerized assessments of cyto-histological specimens have drawn increased attention in the field of digital pathology as the result of developments in digital whole slide scanners and computer hardwares. Due to the essential role of nucleus in cellular functionality, automatic segmentation of cell nuclei is a fundamental prerequisite for all cyto-histological automated systems. In 2D projection images, nuclei commonly appear to overlap each other, and the separation of severely overlapping regions is one of the most challenging tasks in computer vision. In this thesis, we will present a novel segmentation technique which effectively addresses the problem of segmenting touching or overlapping cell nuclei in cyto-histological images. The proposed framework is mainly based upon a statistical level-set approach along with a topology preserving criteria that successfully carries out the task of segmentation and separation of nuclei at the same time. The proposed method is evaluated qualitatively on Hematoxylin and Eosin stained images, and quantitatively and qualitatively on fluorescent stained images. The results indicate that the method outperforms the conventional nuclei segmentation approaches, e.g. thresholding and watershed segmentation.

Acknowledgments

I would first like to express my deepest gratitude to my advisors, Dr. Tien. D. Bui and Dr. Thomas Fevens, for their great support, precious guidance and extensive knowledge. I greatly thank Dr. Bui for the serious effort he put in enlightening me and his other students on advanced topics of computer vision and image processing and providing me with his excellent resources and source codes. I would like to thank Dr. Fevens who has given me the direction and technical support. Under his supervision I became interested in the field of medical image segmentation. I acknowledge my gratitude to my examining committee, Dr. Adam Krzyzak and Dr. Charalambos Poullis for their insightful comments and valuable suggestions.

A special thanks to my dearest friends, Mina Yousefi and MohammadReza Ameri, who were always there for me through the good times and the bad and were always willing to help me with their best suggestions. I would also thank my lab mates Kha Gia Quach and Chi Nhan Duong, who created a friendly and positive atmosphere in our lab and my close friends Parmida Atighehchian and Mahsa Khoshab who always believed in me and all the other people who helped me during this journey.

Most importantly, this dissertation would not have been accomplished without the support of my parents and my younger brother who always encouraged me to do my best. I take this opportunity to thank my family for their comfort and love.

Contents

List of Figures

List of Tables

Chapter 1

Introduction

Pathology is a medical specialty which concerns laboratory examination of cells and tissue samples with the purpose of diagnosis and characterization of diseases. More specifically, cytopathological and histopathological examinations of a biopsy or surgical specimen are two main branches of anatomical pathology that are commonly applied to diagnose various diseases including cancer. Cytopathology (or cytology) refers to the microscopic investigation of samples on the cellular level and is mainly advantageous when quick preparation, staining and interpretation procedures are needed. Despite the fact that cytopathological imagery are highly beneficial as they provide great cellular details with a low cost, cytological examinations alone are not sufficient for accurate diagnosis purposes. For instance, they cannot indicate whether the cancer cells are spreading into and damaging surrounding tissues. Therefore, to obtain a higher diagnostic accuracy, the preliminary cytological tests must be confirmed by the so called histopathological (or histological) assessments for which the overall tissue architecture is evaluated.

Pathologists usually make diagnostic interferences by visual inspection of cells based on their morphological features and architecture, such as shape, position, size, number, etc. Although still being considered as the gold standard, manual examination of biological images is tedious work
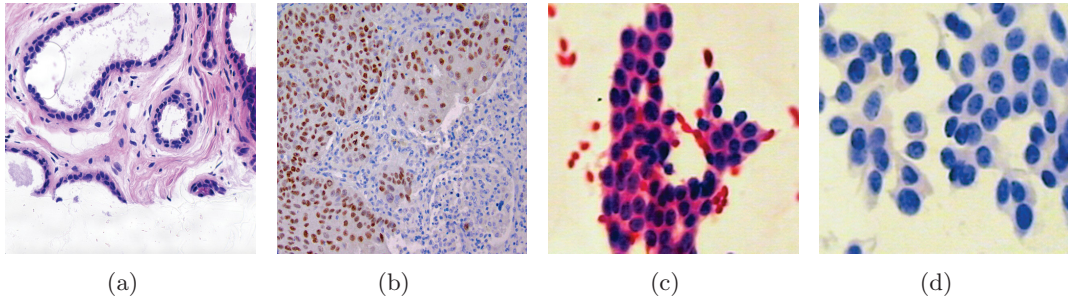
Figure 1.1: Figures (a) and (b) are examples of histopathological imagery while figures (c) and (d) are Cytopathological imagery.

which requires many hours of human labor. This highlights the requirement for an automatic system that accurately measures these features in a few seconds. Recently, computerized methods including automatic detection, segmentation and classification of objects in cyto-histological specimens, have drawn increased attention in the field of digital pathology as the result of developments in digital whole slide scanners and computer hardwares. Due to the essential role of nucleus in cellular functionality, automatic segmentation of cell nuclei is a fundamental prerequisite for all histological and cytological automated systems. Moreover, it substantially facilitates the segmentation of cytoplasms and the surrounding tissues.

Despite the considerable amount of research that has been dedicated to this topic, nuclei segmentation in cyto-histological imagery, is still one of the most challenging tasks for several reasons. First, because of the staining process, the presence of noise is almost ineluctable. Second, final segmentation results may be affected by nonuniform illumination of the image, resulted from the thickness of sample or microscope setup. Finally and most importantly, in 2D projection images, nuclei commonly appear to overlap each other, and the separation of severely overlapping regions is not trivial.

In this thesis, we will present a fully automated unsupervised segmentation technique which effectively addresses the problem of segmenting touching or overlapping cell nuclei in cyto-histological specimens. The rest of this thesis is organized as follows: in chapter (2) we will

review the related literature regarding nuclei detection/segmentation along with the background material on curve evolution and level set technique. In chapter (3) we will extensively describe different stages of the proposed segmentation pipeline. We will also examine the presented method on Hematoxylin and Eosin (H&E) breast images as well as fluorescent imagery in chapter (4). Finally, we will present our concluding remarks in chapter (5).

Chapter 2

Nuclei Localization, Segmentation and Refinement Methodologies

Although a large variety of nuclei segmentation approaches have been recently developed by researchers, their overall strategies typically include the same routines; i.e., Preprocessing, Nuclei detection/localization, Nuclei segmentation and Nuclei Refinement. Nuclei refinement is a post-processing step, which usually refers to the task of detaching the aggregated nuclei or merging the over-segmented nuclei. For instance, in [10], nuclei seeds are first identified using the extended H-maxima transform. Seeds then serve as the starting points in watershed segmentation. Finally, clumps of nuclei are separated using a distance transform, considering the fact that nuclei are fairly round. In [12] nuclei are first segmented from the background using local thresholding. The watershed algorithm is then performed to separate the overlapping nuclei, followed by a remerging step to avoid over-segmentation. In [20] and [21] adaptive thresholding and active contours are utilized respectively to segment the foreground clustered nuclei. Subsequently, distance transform, H-minima transform and watershed algorithm are applied for marker extraction and

nuclei separation.

2.1 Preprocessing

Prior to the main segmentation stage e.g. nuclei detection and segmentation, a few preprocessing steps are normally required to compensate for unfavorable acquisition conditions and inconsistencies in the preparation of slides such as nonuniform illumination, nonuniform color, and noise [7]. The illumination correction can be achieved using either white shading correction or estimating the illumination pattern according to the series of images. Furthermore, many nuclei segmentation approaches perform color normalization in a different color space rather than the conventional RGB color model including HSV, Lab, LUV or MDC [1] [55] . Finally, thresholding, morphological operation and Gaussian smoothing are the common noise reduction methods frequently used in literature.

2.2 Nuclei Detection

Nuclei detection can be regarded as identification of cell nuclei by means of locating the set of points referred to as "seeds" or "markers", normally one per nucleus and close to its center. This step is of great importance because the final segmentation results highly rely on how precisely the initial seeds are determined. Nuclei of most cells are generally rounded or slightly elliptical in shape, as observed in histopathological and cytopathological imagery. Therefore, many nuclei detection techniques in literature have been developed according to the prior knowledge of the nucleus shape. In most cases, nuclei detection involves extracting the local maxima of a response map, where the mapping function highlights regions with certain prior aspects.

---

[1]The Most Discriminant Color Space

Among earlier approaches, Distance Transform [24] has been commonly employed in conjunction with H-maxima/H-minima transforms [10, 13, 20, 21]. The distance transform (DT) is a simple operator which is normally applied to the binarized images. The resulting image is obtained by replacing the intensity of each pixel with its distance from the nearest background pixel. One great drawback of the use of distance transform is being highly sensitive to the noise, thereby leading to over-seeding and over-segmentation.

The classical Hough transform and its variations [25, 27] have been extensively used for nuclei detection [14, 22]. There are several limitations associated with the Hough transform. First, the transform is computationally expensive, being of order $O(KBN)$, where K is the number of pixels in the image, B is the number of circular bins, and N is the width of the neighborhood. Moreover, since the transform is applied to the gradient image, the efficiency of the transform relies on how correctly nuclei edges are extracted. It also means that the transform is sensitive to noise. As an alternative, Radon Transform [17, 26] seems to be more robust to noise, yet it suffers from the lack of efficiency.

In [32], Esteves et al. thoroughly investigated the application of Local Convergence Filters (LCF), initially proposed by [29–31], in nuclei detection. LCF refer to the wide range of filters that are commonly designed to find convex objects as they reveal locations in the image where the gradient vectors converge within a local region (support region).

2.3   Nuclei Segmentation

As mentioned earlier, nuclei segmentation is an essential requirement in computer-aided cyto-histological diagnosis. Generally speaking, image segmentation is the process of subdividing an image into multiple regions or categories, usually with the aim of simplifying further analysis. In this process, each pixel of the image is assigned to one of the available categories such that: (1)
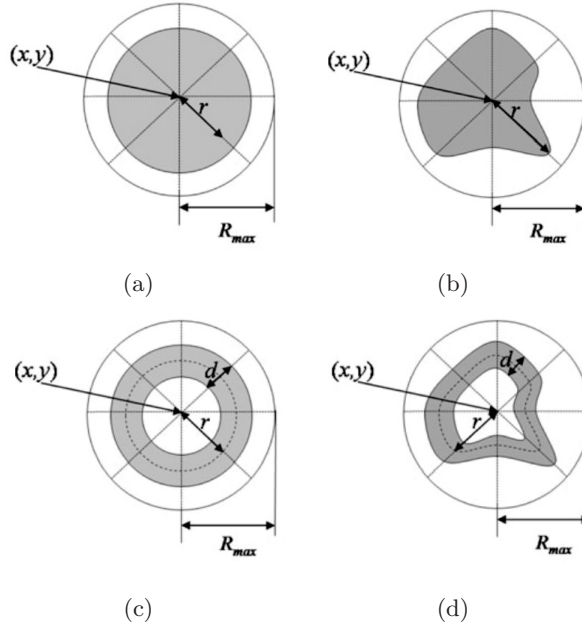
Figure 2.1: Examples of LCF filters represented in [32]; (a) Coin filter [29]; (b) IRIS filter [29]; (c) Adaptive ring filter [30]; (d) Side band filter [31]

pixels that are assigned to the same category have similar characteristics, whereas (2) adjacent pixels assigned to different categories, are disparate from each other regarding to those characteristics. Since the primary concentration of this thesis is on pathology specimen images, only the common segmentation approaches to this area of research are briefly discussed.

Thresholding is the simplest and perhaps the most common segmentation technique that classifies pixels into two categories based on a certain threshold intensity value [11, 12]. Another group of segmentation schemes frequently used in this context, are those ones that mainly rely on morphological operations to perform segmentation [8, 10].

A very common region-based segmentation approach in medical image analysis and particularly in nuclei segmentation, is the so called watershed algorithm which is the method of choice, mainly because of its intrinsic capability of separating overlapping objects [10, 12, 18, 20–22, 44]. For this reason, in the next section we will review a common mathematical definition of watershed, based on the concept of topographical distance [45].

7

2.3.1 Watershed Segmentation Method

Intuitively, a grayscale image can be viewed as a topographic surface in which the elevation of each location in the landscape indicates the intensity value of the corresponding pixel. Assuming that the landscape is gradually being immersed in water, then the catchment basins around the local minima or valleys start to get filled with water. Also, catchment basins are separated from the adjacent catchment by locating a watershed line (or watershed) at the points where water coming from two catchment basins is about to merge. Finally, as the water reaches to the highest point, the process is stopped and the resulting watersheds form the final segmentation boundaries. To be more explicit, let I represent a digital grayscale image, then the lower slope $LS(\mathbf{p})$ of I at pixel $\mathbf{p}$ is defined as:

$$LS(\mathbf{p}) = \max_{\mathbf{q} \in N(\mathbf{p})} \left(\frac{I(\mathbf{p}) - I(\mathbf{q})}{d(\mathbf{p}, \mathbf{q})} \right) \tag{2.1}$$

where $N(\mathbf{p})$ denotes the neighbors of pixel $\mathbf{p}$ including $\mathbf{p}$, and $d(\mathbf{p}, \mathbf{q})$ is the Euclidean distance between pixels $\mathbf{p}$ and $\mathbf{q}$. Also, when $\mathbf{p} = \mathbf{q}$ the lower slope is defined to be zero. Accordingly, the set of lower neighbors of pixel $\mathbf{p}$ denoted by $\Gamma(\mathbf{p})$ is:

$$\Gamma(\mathbf{p}) = \left\{ \mathbf{q} \in N(\mathbf{p}) \ \middle| \ \frac{I(\mathbf{p}) - I(\mathbf{q})}{d(\mathbf{p}, \mathbf{q})} = LS(\mathbf{p}) \right\} \tag{2.2}$$

Pixel $\mathbf{q}$ is said to belong to the upstream of pixel $\mathbf{p}$, if there exists a path $\pi = (\mathbf{p}_0, .., \mathbf{p}_l)$ of steepest slope from $\mathbf{p}_0$ to $\mathbf{p}_l$, that means: $\forall i = 0, .., l-1, \mathbf{p}_{i-1} \in \Gamma(\mathbf{p}_i)$. For each local minima m_i in the image, the corresponding catchment basin $CB(m_i)$ is the set of all points in the

upstream of m_i. Finally, watershed pixels are the pixels for which there is at least two paths of steepest slope toward different local minima.

Despite its simplicity, high speed and inclusive segmentation, the traditional watershed transform has the major drawback of over-segmentation, since the method is highly sensitive to noise and irrelevant local minima. Thus several alternatives such as marker controlled watersheds and hierarchical watersheds have been developed to improve the method. A comprehensive study of different watershed definitions and algorithms can be found in [46].

While there have been various attempts on the field of nuclei segmentation in literature, optimization techniques are being considered as more principled, systematic and flexible methods. Generally speaking, these methods may be categorized mainly into spatially discrete and spatially continuous settings. In the discrete setting, the input image is converted into a directed graph such that pixels of the image are treated as the graph nodes and the segmentation is obtained by means of finding the minimal (cost) cut in the graph. Continuous optimization methods, on the other hand, aim at minimizing an energy functional which mostly involves solving partial differential equations. In what follows, we will briefly discuss some major contributions to this field.

2.4   Curve Evolution and Level Set Techniques

In the variational frameworks, the segmentation of an image $u_C : \Omega \in \mathbb{R}^2 \rightarrow \mathbb{R}$ is achieved through the minimization of an appropriate energy functional subject to some constraints, in such a way that the local or global minima occurs at the boundary of the desired objects. This is obtained by deforming a closed curve $C : [0 \ 1] \rightarrow \Omega$ in the direction of negative energy gradient, described by the following gradient descent:

$$\frac{\partial C}{\partial t} = -\frac{\partial E(C)}{\partial C} \tag{2.3}$$

Here, the evolution of the curve is expressed in an explicit manner. Using the alternative implicit representation, in which contours are regarded as the zero level curve of some embedding function ϕ:

$$C = \{(x, y) \in \Omega \mid \phi(x, y) = 0\} \tag{2.4}$$

one can reformulate equation (2.3) as:

$$\frac{\partial \phi}{\partial t} = -\frac{\partial E(\phi)}{\partial \phi} \tag{2.5}$$

The level set methods originally developed by Osher and Sethian [37] are conceptually simple, yet powerful mathematical tools for numerically analyzing and computing the motion of curves and surfaces. The level set approach suggests that rather than directly evaluating the motion of a curve in the plane, we can find an embedding surface such that at each time, the evolving curve exactly fits the intersection between the moving surface and the $x - y$ plane Fig.(2.2.a). For this reason, the curve is commonly referred to as the zero level-set or zero level-curve of the
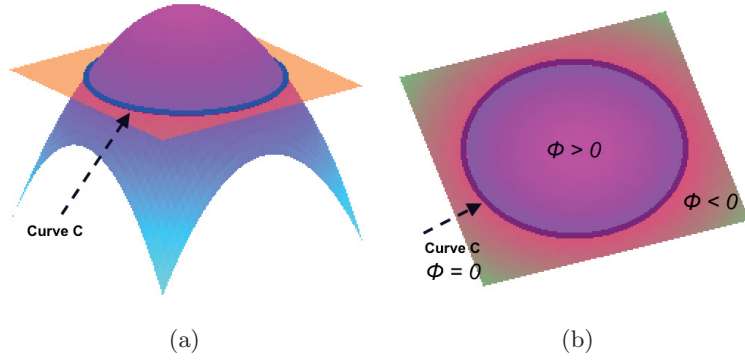
10

(a)   (b)

Figure 2.2: Illustration of level set function in 3D space.

surface.

To be more precise, through the introduction of a Lipschitz continuous function $\phi(x, y, t)$: $\Omega \to \mathbb{R}$, the level set representation of a curve is given as follows:

$$C = \{(x, y) \in \Omega \mid \phi(x, y) = 0\}, \qquad \begin{cases} \phi(x, y, t) = 0 & \text{on the curve} \\ \\ \phi(x, y, t) > 0 & \text{inside the curve} \\ \\ \phi(x, y, t) < 0 & \text{outside the curve} \end{cases} \qquad (2.6)$$

One typical example of such function is the signed distance function of curve.

Level set based techniques have become increasingly popular in the field of Geometric PDEs [2] and variational image segmentation, as they bring several advantages: In case of 2D plane curves, calculations are done in a fixed rectangular grid, making the level set formulation perfectly suited for dealing with gray level images. Moreover, unlike the explicit parametrization methods, they can handle the automatic changes in topology i.e. merging and splitting of the segmented regions. Further, the issue of self-intersection of curves in parametric deformable models no longer exists.

---

[2]Partial Differential Equations

2.4.1 Edge-Based and Region-Based Active Contours

Earlier works in the variational framework were mainly based upon the classical Snakes, also called active contours models [33]:

$$E(C) = -\int |\nabla I(C)|^2 ds + \nu_1 \int |C_s|^2 ds + \nu_2 \int |C_{ss}|^2 ds \qquad (2.7)$$

Where parameter s is the arc-length along the curve and C_s and C_{ss} stand for the first and second derivate of the curve with respect to s. One main difficulty of using the explicit representation of Snakes in (2.7) is that they are not capable of handling the topological changes; therefore not capable of detecting multiple objects in the image simultaneously. Besides, because of the explicit parametrization of the evolution, a re-parameterization procedure is required every few iterations. With some slight modifications, the Geodesic Active Contours model [34] proposed a level-set formulation for the Snake model, which resolves the issues arising from the explicit parametrization:

$$\begin{aligned}
\frac{\partial \phi}{\partial t} &= |\nabla \phi| \ div \ \big(g(I)\frac{\nabla \phi}{|\nabla \phi|}\big) \\
&= g(I)|\nabla \phi| \ div \ \big(\frac{\nabla \phi}{|\nabla \phi|}\big) + \nabla g(I).\nabla \phi
\end{aligned} \qquad (2.8)$$

The classical snakes and the geodesic active contours are considered as "edge-based" active contours as they both rely on an edge detector function (of $|\nabla I|$) to stop the evolving curve. As a result, they can only detect objects with distinct boundaries. Also, since they are locally optimized the segmentation result highly depends on the initialization and there is always a

high chance of getting trapped in the false local minimum. Furthermore, in cases with complex topology e.g. multiple holes and bridges, the edge-based active contours will not suffice to properly segment the image. In contrast to the "edge-based" methods that mainly depend on local features such as gradient, "region-based" active contours use the global or regional information of the image for the stopping procedure which makes them more robust to noise compared with the edge-based techniques. In this context, the Mumford-Shah (MS) energy model [35] and its well-established piecewise constant approximation, also known as "Cartoon Limit", have been broadly used as the region-based variational approaches to the task of image segmentation.

In Mumford-Shah model, segmentation of a given image $u_C : \Omega \in \mathbb{R}^2 \to \mathbb{R}$ into a number of sub-regions is considered as the problem of computing the optimal piecewise smooth approximation $u : \Omega \to \mathbb{R}$ of the image, such that u varies smoothly or slowly within each region, and it varies discontinuously or rapidly across the boundaries of the regions. Accordingly, the piecewise smooth approximation is obtained by minimizing the following energy functional:

$$E^{MS}(u, C) = \int_{\Omega \backslash C} |u - u_C|^2 dxdy + \mu \int_{\Omega \backslash C} |\nabla u|^2 dxdy + \nu |C| \qquad (2.9)$$

Where constants $\mu \geq 0$ and $\nu \geq 0$ are weighting parameters, C is the boundary of an open subset ω of Ω, i.e. $\omega \in \Omega$ and $C = \partial \omega$, and the total length of the boundaries of regions $|C|$, penalizes the smoothness of the segmentation curve. If we assume that the segmentation curve C partitions image into two regions u_1 and u_2 referring to inside the curve and outside the curve, i.e. foreground and background regions, equation (2.9) can be re-written as follows:

$$E^{MS}(u_1, u_2, C) = \int_{inside\ C} |u_1 - u_C|^2 dxdy + \mu_1 \int_{inside\ C} |\nabla u_1|^2 dxdy$$

$$+ \int_{outside\ C} |u_2 - u_C|^2 dxdy + \mu_2 \int_{outside\ C} |\nabla u_2|^2 dxdy + \nu|C| \tag{2.10}$$

The numerical analysis of MS equation was facilitated by the level-set method which can be found in [38] in more details. Accordingly, the level set representation of the above equation can be written as:

$$E^{MS}(u_1, u_2, \phi) = \int |u_1 - u_C|^2 H(\phi) dxdy + \mu_1 \int |\nabla u_1|^2 H(\phi) dxdy$$

$$+ \int |u_2 - u_C|^2 (1 - H(\phi)) dxdy + \mu_2 \int |\nabla u_2|^2 (1 - H(\phi)) dxdy + \nu \int |\nabla H(\phi)| dxdy. \tag{2.11}$$

Where $H(z)$ is the Heaviside function of variable z:

$$H(z) = \begin{cases} 1 & \text{if} \quad z \geq 0 \\ 0 & \text{if} \quad z < 0 \end{cases} \tag{2.12}$$

The Mumford-Shah paradigm in its original form has a nontrivial solution that requires much computation time because it involves solving three Euler-Lagrange equations simultaneously [38]. As an alternative, Chan and Vese in [39] proposed a piecewise constant model along with its level-set formulation and demonstrated that the model is equivalent to the two-phase piecewise constant approximation of MS. Assuming that image u_C is composed of two regions u_1 and u_2 having constant intensities c_1 and c_2 respectively, the "Chan-Vese" (CV) model is written as:

$$E^{CV}(c_1, c_2, C) = \lambda_1 \int_{inside\ C} |c_1 - u_C|^2\ dxdy + \lambda_2 \int_{outside\ C} |c_2 - u_C|^2\ dxdy$$

$$+\nu\ .\ Length(C).$$

$$(2.13)$$

Using the level set framework, the above energy can be written as:

$$E^{CV}(c_1, c_2, \phi) = \lambda_1 \int_{\Omega} |c_1 - u_C|^2\ H(\phi(x,y))\ dxdy + \lambda_2 \int_{\Omega} |c_2 - u_C|^2\ (1 - H(\phi(x,y)))\ dxdy$$

$$+\nu \int_{\Omega} \delta(\phi(x,y))\ |\nabla\phi(x,y)|\ dxdy.$$

$$(2.14)$$

Where, $H(\cdot)$ and $\delta(\cdot)$ respectively denote the Heaviside function defined in equation (2.12) and one-dimensional Dirac delta function, i.e. $\delta(z) = dH(z)/dz$. The Gradient descent equations of the above functional are then formed by employing the Euler-Lagrange derivation:

$$\frac{\partial\phi}{\partial t} = \delta(\phi)[-(c_1 - u_c)^2 + (c_2 - u_c)^2 + \nu\ div(\frac{\nabla\phi}{|\nabla\phi|})].$$

$$(2.15)$$

$$c_1(\phi) = \frac{\int_{\Omega} u_c(x,y)H(\phi(x,y))\ dxdy}{\int_{\Omega} H(\phi(x,y))\ dxdy}.$$

$$(2.16)$$

$$c_2(\phi) = \frac{\int_{\Omega} u_c(x,y)(1 - H(\phi(x,y)))\ dxdy}{\int_{\Omega}(1 - H(\phi(x,y)))\ dxdy}.$$

$$(2.17)$$

A possible regularization of functions $H(\cdot)$ and $\delta(\cdot)$ is suggested by [39]:

15

$$H(z) = \frac{1}{2} + \frac{1}{\pi} \ arctan \ (\frac{z}{\epsilon}). \quad , \quad \delta(z) = \frac{dH(z)}{dz}. \tag{2.18}$$

Where ϵ is a small number.

2.4.2 Optimum Choice of Smoothness Parameter

The smoothness parameter has a critical role in segmentation results. Choosing very small values of ν will lead to over segmentation, since small edges created by the noise are also segmented. On the other hand, choosing very large values of ν will not produce some of the important edges. In [54], the optimum choice of parameter ν is suggested to be:

$$\nu = \beta\sigma^2 \tag{2.19}$$

$$\sigma^2 = \frac{\int_\Omega (u - \bar{u})^2 dxdy}{\int_\Omega dxdy} \tag{2.20}$$

Where, σ^2 denotes the variance of image u, $\bar{u}$ is the mean value of u and β is a constant factor which depends on the amount of noise in the original image.

In this chapter, several significant contributions to the field of nuclei detection and segmentation have been briefly discussed. Moreover, some relevant background information considering the basic mathematical concepts of curve evolution and level-set method was given to provide more insight to the reader. As highlighted earlier, optimization techniques such as level-set based methods are being considered as more principled and adaptable methods. However, in the context of nuclei segmentation, a two-phase level set model will not suffice to segment individual nucleus unless a segregation strategy is applied. In the proposed framework, we will add two

16

constraints to the original level-set framework, namely topology preserving constraint and shape constraint. In the succeeding chapter, these constraints will be discussed in details.

Chapter 3

The Proposed Framework

The proposed framework is a new region-based segmentation method, which consists of three major modules. First, to extract the desired stains, the image is passed through a color deconvolution unit [3]. Afterward, the generalized fast radial symmetry transform, also known as GFRS [5], followed by non-maxima suppression is used to specify the initial seed points and their corresponding GFRS ellipses. Later, the resulting ellipses, which may be interpreted as the initial nuclei borders (one per nucleus) serve as the initial curves in a level-set variational framework. Finally, nuclei borders are evolved through the use of a statistical level-set approach along with a topology preserving criteria that successfully carries out the task of segmentation and separation of nuclei at the same time. Indeed, the topology preserving constraint [6] prevents the evolving regions from remerging into each other. The flow chart in figure (3.1) demonstrates the presented framework.
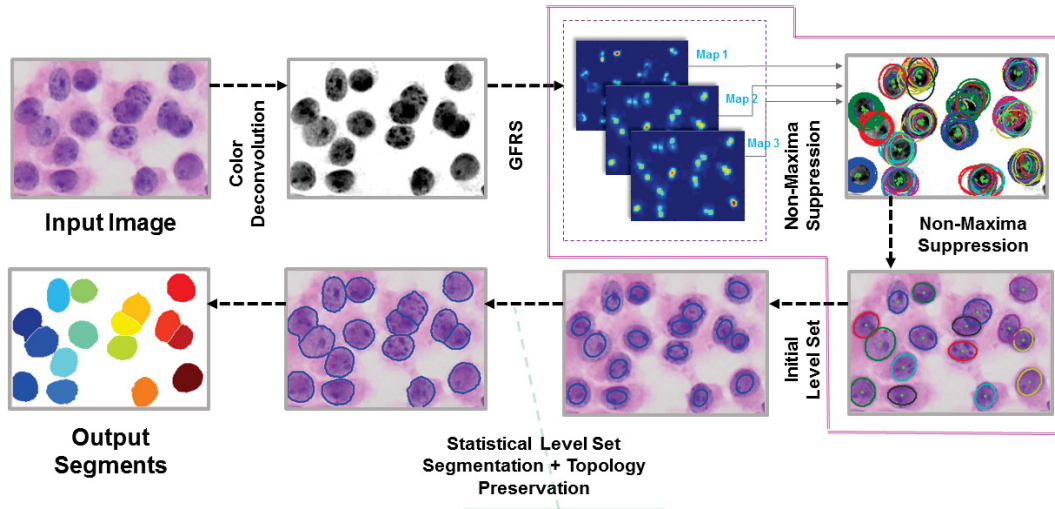
Figure 3.1: Nuclei Segmentation Pipeline for H&E images

3.1 Color Deconvolution

In order to improve the visualization of cell and tissue sections and highlight the desired structures, biological specimens are usually stained with certain number of dyes. The most widely used staining protocol is the combination of Hematoxylin and Eosin (H&E). Hematoxylin stains nuclei blue, whereas Eosin is employed to stain red blood cells, cytoplasm and extracellular structures magenta or red. Whole slide digital scanners currently available use the RGB-based[1] imaging sensors, thus a stain separation method is needed to calculate the contribution of each stain. Ruifrok and Johnston in [3] proposed an unmixing algorithm for up to three stains that reveals uncorrelated information about stain concentration even when the stains have overlapping spectral absorption. According to Lambert-Beers law, the gray level of channel C is exponentially dependent on the stain concentration:

---

[1]Red-Green-Blue

19

$$I_C = I_{0,C} exp(-A\ c_C) \tag{3.1}$$

Where $I_{0,C}$ and I_C are intensity of light, before and after passing through the sample slide, A is the amount of stain, and c_C is the absorption factor of stain for intensity channel C. The optical density (OD) of channel C is then defined as:

$$OD_C = -log_{10}(I_C/I_{0,C}) = A\ c_C \tag{3.2}$$

For each stain, optical densities of RGB channels can be measured in advance according to the above equation. Given these reference optical densities, each stain can be characterized by a 3×1 vector, $OD = [s_r\ s_g\ s_b]^T$. After dividing each OD vector by its total length, the normalized OD matrix, $\mathbf{S}$, can be formed:

$$\mathbf{S} = \begin{array}{c} \\ \\ \\ \end{array} \begin{matrix} stain\ 1 & stain\ 2 & stain\ 3 \\ \left(\begin{matrix} s_{r,1} & s_{r,2} & s_{r,3} \\ s_{g,1} & s_{g,2} & s_{g,3} \\ s_{b,1} & s_{b,2} & s_{b,3} \end{matrix} \right) & \begin{matrix} R \\ G \\ B \end{matrix} \end{matrix}$$

If we assume that $\mathbf{X}$ is a 3×1 vector containing the amount of each stain at a particular pixel (x, y), then the OD values $\mathbf{Y}$ at that pixel can be calculated from the following linear equation:

$$\mathbf{Y}(x, y) = \mathbf{S}\ \mathbf{X}(x, y), \tag{3.3}$$

20

Finally, solving the above linear equation yields in a 3×1 vector representing the amount of stains s_1, s_2, s_3 at pixel (x, y):

$$\mathbf{X}(x, y) = \mathbf{S}^{-1}\mathbf{Y}(x, y) = \mathbf{D}\mathbf{Y}(x, y) \tag{3.4}$$

In particular, for the combination of Hematoxylin, Eosin and DAB stains, D is:

$$\mathbf{D} = \begin{pmatrix} 1.88 & -1.02 & -0.55 \\ -0.07 & 1.13 & -0.13 \\ -0.6 & -0.48 & 1.57 \end{pmatrix}$$

Figures (3.2) and (3.3) illustrate two examples of Hematoxylin and Eosin stained tissues and their corresponding stain separation results acquired by the above method.

3.2 Noise Reduction and Contrast Enhancement

As previously mentioned, in cyto-histological images noise is mainly considered as the undesirable structures that appear in the background due to the staining and imaging process. Hence, objects that are small enough to be considered as noise will be removed after the segmentation stage through the use of morphological opening. Furthermore, choosing higher values of smoothness
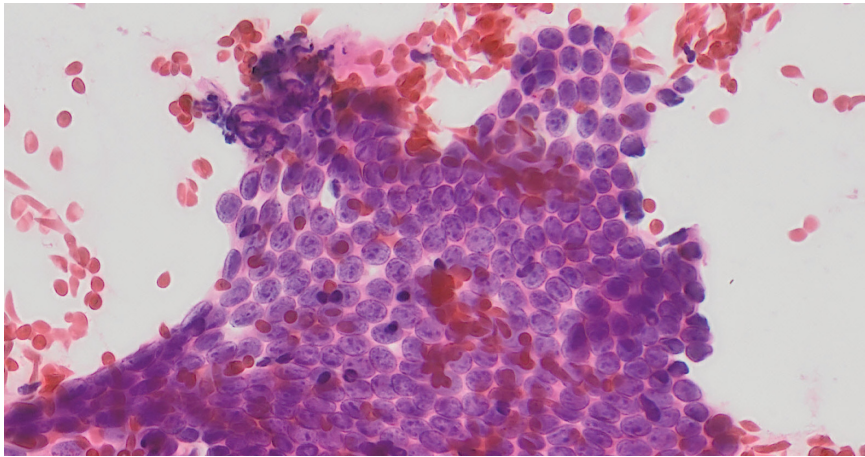
(a)
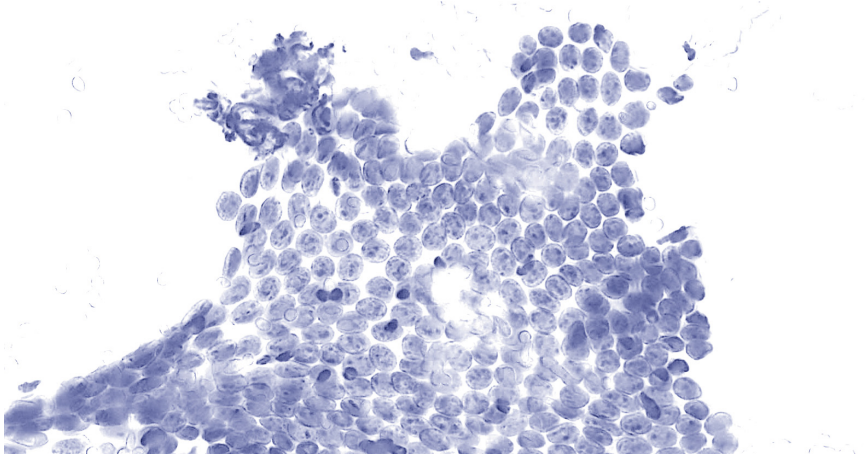
(b)
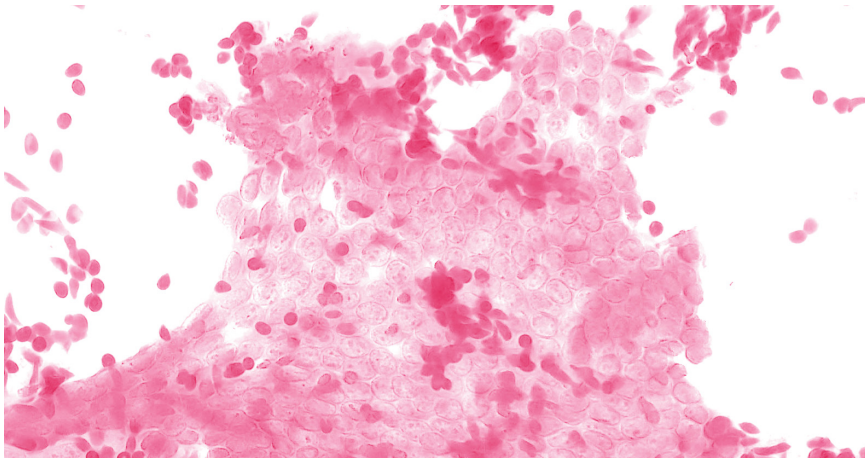
(c)

Figure 3.2: Examples of H&E stain separation using color deconvolution [3] (a) Original RGB image. (b) Hematoxylin. (c) Eosin.

(a)

(b)

(c)

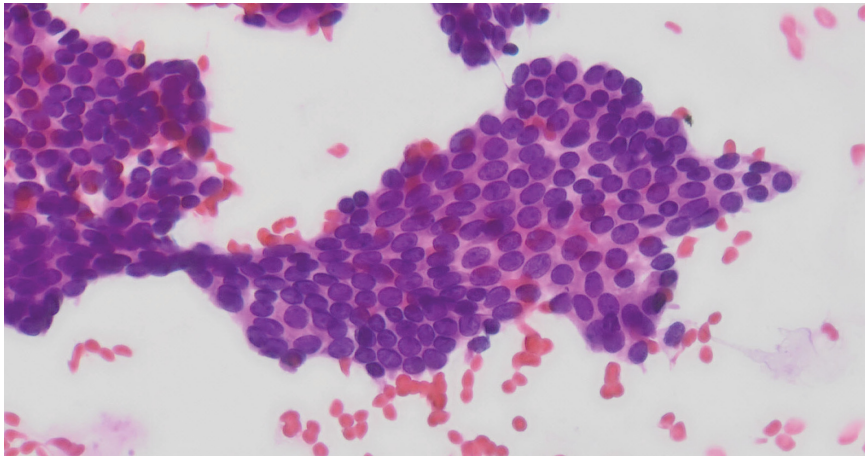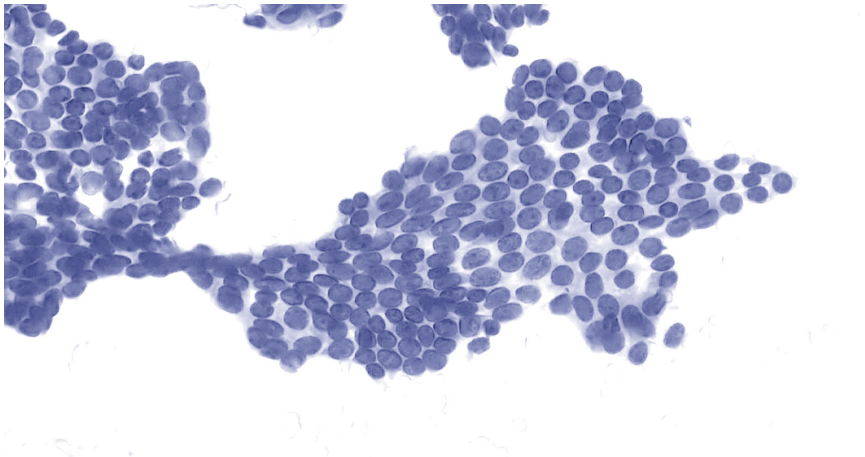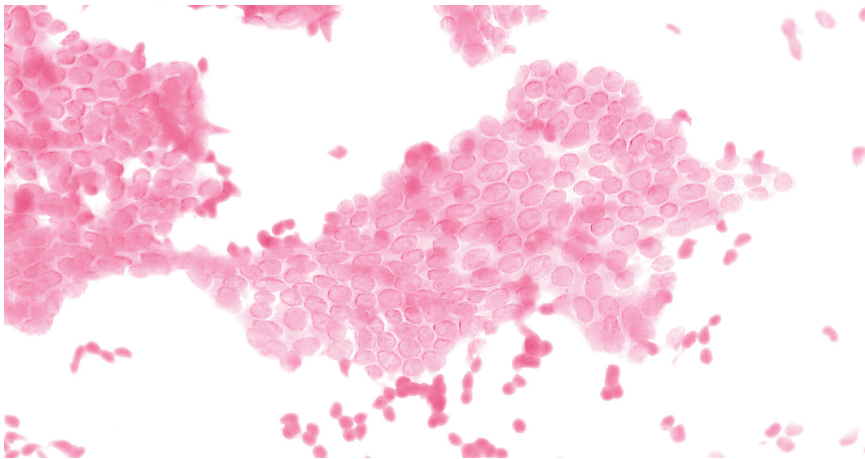Figure 3.3: Examples of H&E stain separation using color deconvolution [3] (a) Original RGB image. (b) Hematoxylin. (c) Eosin.

parameter (which will be introduced later in section (2.3)) will automatically lead to the elimination of small structures. Aside from that, because of intrinsic acquisition mechanism in CCD [2] sensors, microscopic images may contain some level of Poisson noise. In order to reduce this type of noise, (isotropic) nonlinear diffusion filtering has been used to smooth the image while preserving or even enhancing the sharp edges. Assuming that $I(x, y)$ and Ω be the original image and image domain, $u(x, y, t)$, the solution of diffusion equation is calculated using the following diffusion equation:

$$\partial_t u = div \ (g(|\nabla u_\sigma|^2)\nabla u) \tag{3.5}$$

where,

$$u(x, y, 0) = I(x, y). \tag{3.6}$$

$$\partial_n u = 0 \ , \quad on \ \ \partial\Omega \tag{3.7}$$

Here, **n** denotes the normal vector of image boundary $\partial\Omega$, t is a scaling parameter, and the diffusivity function g is a decreasing function of gradient magnitude $|\nabla u_\sigma|$, where u_σ is a Gaussian smoothed version of u. A semi-implicit discretization scheme i.e. Additive Operator Splitting (AOS) has been used to obtain more stable and faster result. More details about the AOS scheme can be found in [53]. In order to enhance image contrast, a linear gamma correction method has been used such that one percent of data is saturated at low and high intensities.

---

[2]Charge-Coupled Device

3.3 Nuclei Detection

As for nuclei detection previously discussed in section (2.2), the fast radial symmetry transform and its affine invariant variation are employed. In the following subsections, these methods will be described in detail.

3.3.1 Fast Radial Symmetry

The fast radial symmetry (FRST) has been very popular due to its good performance in detecting the points of high radial symmetry, while preserving low computational cost and complexity [4]. Thanks to its fast runtime and high efficiency, FRST has been widely used in real time applications, e.g. object tracking. The transform can be explained in the following way:

For each image pixel $\boldsymbol{p}$, and each radius $n \in N$, the corresponding *positively-affected* $\boldsymbol{p}_{+ve}(\boldsymbol{p})$ and *negatively-affected* $\boldsymbol{p}_{-ve}(\boldsymbol{p})$ pixels are defined as the pixels a distance n away from $\boldsymbol{p}$ in the direction that the gradient vector at $\boldsymbol{p}$ is pointing to or pointing away from:

$$\boldsymbol{p}_{\pm ve}(\boldsymbol{p}) = \boldsymbol{p} \pm round(\frac{g(\boldsymbol{p})}{||g(\boldsymbol{p})||}n) \tag{3.8}$$

Using affected points $\boldsymbol{p}_{+ve}(\boldsymbol{p})$ and $\boldsymbol{p}_{-ve}(\boldsymbol{p})$, the *orientation projection image* O_n and *magnitude projection image* M_n are formed:

$$O_n(\boldsymbol{p}_{\pm ve}(\boldsymbol{p})) = O_n(\boldsymbol{p}_{\pm ve}(\boldsymbol{p})) \pm 1 \tag{3.9}$$

$$M_n(\boldsymbol{p}_{\pm ve}(\boldsymbol{p})) = M_n(\boldsymbol{p}_{\pm ve}(\boldsymbol{p})) \pm ||g(\boldsymbol{p})|| \tag{3.10}$$
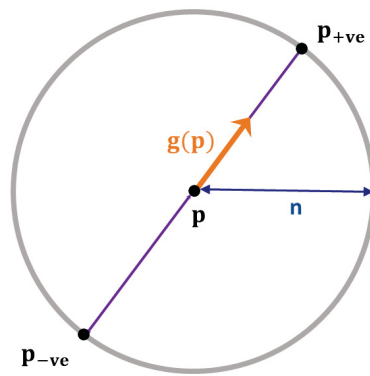
(a)
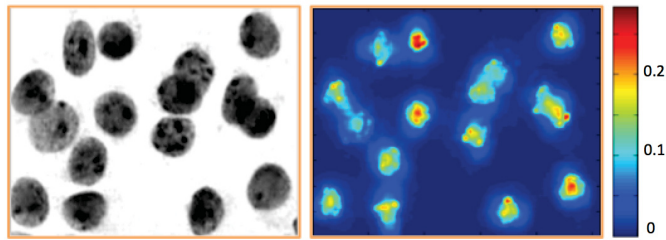
(b)

Figure 3.4: Fast Radial Symmetry Transform: (a) Point $\boldsymbol{p}$ and the corresponding affected pixels $\boldsymbol{p}_{+ve}$ and $\boldsymbol{p}_{-ve}$ shown with black dots. (b) A grayscale image and its FRST transform.

Where O_n and M_n are initially zero. At each positively affected point, images O_n and M_n are incremented by 1 and $||g(\boldsymbol{p})||$ respectively and at each negatively affected point, O_n and M_n are decremented by the same quantities. Finally, radial symmetry transform at radius n is defined as the convolution:

$$S_n = F_n * A_n \tag{3.11}$$

Where A_n is a Gaussian kernel, F_n and $\tilde{O}_n$ are:

$$F_n(\boldsymbol{p}) = \frac{M_n(\boldsymbol{p})}{k_n} \left(\frac{|\tilde{O}_n(\boldsymbol{p})|}{k_n} \right)^{\alpha} \qquad \tilde{O}_n = \begin{cases} O_n(\boldsymbol{p}) & if \;\; O_n(\boldsymbol{p}) < k_n \\ \\ k_n & otherwise \end{cases} \tag{3.12}$$

and k_n and α are the scaling factor at radius n and radial strictness parameter respectively. The total transform over a set of radii $N = \{n_1, n_2, ...\}$ is defined as the average of all radially symmetric transforms S_n, $n \in N$.

3.3.2 Generalized Fast Radial Symmetry Transform

Cell nuclei vary in size and shape during different phases of metabolism. Moreover, they may deviate significantly from spherical symmetry in response to many different factors. For instance, it has been observed that diseases like cancer may cause significant elongation in nuclei shape. Therefore, in order to precisely locate the cell nuclei, it is necessary to incorporate techniques that can handle the elongation in shape of the nuclei. For this reason, in addition to the circular symmetry approximation, it is reasonable to assume that each nucleus in the image has undergone an affine transformation.

Although the fast radial symmetry (FRS) has been regarded as an efficient method which provides impressive results with a relatively low computational cost, it is not invariant with respect to the affine transformations. In [5] the fast radial symmetry was extended to the generalized fast radial symmetry (GFRS) for affine invariance systematically by considering the rotation and scaling matrices:

$$R = \begin{pmatrix} \cos(\theta) & -\sin(\theta) \\ \sin(\theta) & \cos(\theta) \end{pmatrix}, \quad S = \begin{pmatrix} a & 0 \\ 0 & b \end{pmatrix} \tag{3.13}$$

Where θ, a, b denote the orientation, major and minor axes respectively. Accordingly, the total affine transformation matrix G and the voting vector $\hat{V}$ are determined:

$$G = R \ S \tag{3.14}$$

$$\hat{V} = G \ M \ G^{-1} \ M^{-1} \ g(\boldsymbol{p}) \ , \quad M = \begin{pmatrix} 0 & 1 \\ -1 & 0 \end{pmatrix} \tag{3.15}$$

In the same manner with (3.8), the associated affected pixels are formed as stated in [5], merely by replacing the gradient vector with the voting vector at point $\boldsymbol{p}$:

$$\boldsymbol{p}_{\pm ve}(\boldsymbol{p}) = \boldsymbol{p} \pm round(\frac{\hat{V}(\boldsymbol{p})}{||\hat{V}(\boldsymbol{p})||}n) \tag{3.16}$$

28

3.4 Nuclei Segmentation

In section (2.3), two commonly used region-based models, namely, piecewise smooth and piecewise constant models were discussed. In a more general manner, segmentation is perceived as a statistical estimation problem. The following sections present a comprehensive overview of the statistical scheme.

3.4.1 Statistical Approach to Level Set Segmentation

The segmentation problem can be addressed within the framework of Bayesian inference by maximizing a posterior probability. Assuming that $\mathcal{P}(\Omega)$ represents the optimal partition of the image $u : \Omega \rightarrow \mathbb{R}$ into disjoint regions: $\Omega_1, ..., \Omega_N$, the Bayes' rule suggests that [40]:

$$p(\mathcal{P}(\Omega)|u) \propto p(u|\mathcal{P}(\Omega)) \; p(\mathcal{P}(\Omega)). \tag{3.17}$$

Where the conditional probability $p(u|\mathcal{P}(\Omega))$, represents the image information based on the partitioning $\mathcal{P}(\Omega)$, whereas the second term is the a-priori probability of the optimal partitioning $\mathcal{P}(\Omega)$ which corresponds to the geometric aspects of the partition and shape priors. Although the statistical scheme allows for complex shape priors, the most typical assumption about the geometric properties of the partition is that the boundary C of the partition is as short as possible. This can be expressed in an exponential form:

$$p(\mathcal{P}(\Omega)) \propto e^{-\nu|C|} \qquad \nu > 0. \tag{3.18}$$

As mentioned earlier, the optimal partition $\mathcal{P}(\Omega)$ splits the image domain Ω into mutually exclusive regions $\{\Omega_1, .., \Omega_N\}$. Further, assuming that different locations (x, y) within the same region Ω_i are independent and identically distributed with the probability density function p_i, the posterior probability $p(u|\mathcal{P}(\Omega))$ can be extended to:

$$
\begin{aligned}
p(u|\mathcal{P}(\Omega)) = p(u|\{\Omega_1, ..., \Omega_N\}) &= \prod_{i=1}^{N} p(u|\Omega_i) \\
&= \prod_{i=1}^{N} \prod_{(x,y)\in\Omega_i} (p_i(u(x,y)))^{dxdy}.
\end{aligned} \tag{3.19}
$$

Rather than directly maximizing the posterior probability, it is more feasible to minimize its negative logarithm that can be expressed as the following energy functional, according to Eqs. (3.17-3.19):

$$E(\{\Omega_i\}_{i=1,..,N}) = -\sum_{i=1}^{N} \int_{\Omega_i} log \ p_i(u(x,y)) \ dxdy + \nu \ |C|. \tag{3.20}$$

3.4.2 Investigation of the Model in Two-Phase Setting

In the two-phase case, in which the image u is assumed to be partitioned into two disjoint regions, Eq. (3.20) comes down to the following energy functional:

$$E(u, C) = \int_{\Omega} -log \ p_1(u(x, y)) \ dxdy + \int_{\Omega \backslash C} -log \ p_2(u(x, y)) \ dxdy + \nu \ |C|. \qquad (3.21)$$

Pursuing the level set scheme, in a similar manner as in the previous section, the level-set representation of the above functional:

$$E(\phi) = \int_{\Omega} -H(\phi(x, y)) \ log \ p_1(u(x, y))$$

$$-(1 - H(\phi(x, y)) \ log \ p_2(u(x, y)) + \nu \ |\nabla H(\phi(x, y))| \ dxdy. \qquad (3.22)$$

and the corresponding gradient descent:

$$\frac{\partial \phi}{\partial t} = \delta(\phi) \big(log \ \frac{p_1(u(x, y))}{p_2(u(x, y))} + \nu \ div \frac{\nabla \phi}{|\nabla \phi|} \big) \qquad (3.23)$$

are formed, where functions $H(\cdot)$ and $\delta(\cdot)$ have been introduced earlier in this chapter.

To further narrow down the statistical approach, the probabilistic model p_i needs to be specified. One may differentiate between parametric and non-parametric probabilistic models. Given a parametric model p_i with a set of parameters θ_i the energy functional in Eq. (3.20) can be expressed as:

$$E(\{\Omega_i, \theta_i\}_{i=1,..,N}) = -\sum_{i=1}^{N} \int_{\Omega_i} log \ p(u(x, y)|\theta_i) \ dxdy + \nu \ |C|. \qquad (3.24)$$

A reasonable choice of such parametric models is the Gaussian distribution function with parameters μ_i and σ_i^2:

$$p(s \mid \mu_i, \sigma_i^2) = \frac{1}{\sqrt{2\pi}\sigma_i} \, exp \, (-\frac{(s - \mu_i)^2}{2\sigma_i^2}) \tag{3.25}$$

Consequently, the gradient descent in Eq. (3.23) will be rearranged into:

$$\begin{aligned}
\frac{\partial \phi}{\partial t} &= \delta(\phi)\big(\, log \, \frac{p(u(x,y) \mid \mu_1, \sigma_1^2)}{p(u(x,y) \mid \mu_2, \sigma_2^2)} + \nu \, div \frac{\nabla \phi}{|\nabla \phi|} \, \big) \\
&= \delta(\phi)\big(\frac{(u(x,y) - \mu_2)^2}{2\sigma_2^2} - \frac{(u(x,y) - \mu_1)^2}{2\sigma_1^2} + log \, \frac{\sigma_2}{\sigma_1} + \nu \, div \frac{\nabla \phi}{|\nabla \phi|} \, \big)
\end{aligned} \tag{3.26}$$

In addition to the parametric models such as Gaussian approximation, non-parametric density estimates are also applicable to the statistical segmentation scheme. As pointed out by [42], the Parzen density estimate p_i, can be simply obtained by smoothing the discrete histogram of region Ω_i, with a Gaussian kernel K_σ:

$$p_i(s) = K_\sigma * \frac{\int_{\Omega_i} \delta_{u(x,y) \, s} \, dxdy}{\int_{\Omega_i} dxdy} \tag{3.27}$$

where $\delta_{ij} = 1$ if $i = j$ and 0 otherwise.

3.4.3   Integrating Multiple Feature Channels

The main advantage of the statistical approach is that the Bayesian framework in Eq. (3.17) is not restricted to the use of image intensity, but rather it can be extended to other image features ,e.g. color, texture, motion, etc. More precisely, image $u : \Omega \to \mathbb{R}$ in Eq. (3.20) can be generally replaced with a feature $F : \Omega \to \mathbb{R}$:

$$E(\{\Omega_i\}_{i=1,..,N}) = -\sum_{i=1}^{N} \int_{\Omega_i} log \ p_i(F(x,y)) \ dxdy + \nu \ |C|. \qquad (3.28)$$

More interestingly, it further allows for integration of multiple cues, in cases where only one cue is not adequate [42]:

$$E(\{\Omega_i\}_{i=1,..,N}) = -\sum_{j=1}^{M}\sum_{i=1}^{N} \int_{\Omega_i} log \ p_{ij}(F_j(x,y)) \ dxdy + \nu \ |C|. \qquad (3.29)$$

where M denotes the number of feature channels and p_{ij} represents the probability density function of feature F_j within region Ω_i.

3.4.4 Statistical Interpretation of Mumford-Shah Model

The gradient descent in Eq. (3.26) indicates a close similarity to the piecewise constant solution in Eq. (2.15). Letting $\mu_1 = c_1$, $\mu_2 = c_2$ and $\sigma_1 = \sigma_2 = \sqrt{0.5}$, the Gaussian Bayesian model comes down exactly to the piecewise constant approximation of the Mumford-Shah i.e. cartoon model. In other words, the cartoon model is equivalent to the Gaussian probabilistic model with a fixed standard deviation. Brox and Cremers in [41] further illustrated that the piecewise smooth Mumford-Shah is a first order approximation of the Bayesian model with local region statistics. In contrast to the previously mentioned statistical models where the same probability density function is applied to all the locations within a region; local region models consider a different probability density for each location of a region. The Gaussian distribution corresponding to the local setting leads to:

$$p_i(s, x, y) = \frac{1}{\sqrt{2\pi}\sigma_i(x, y)} \ exp \ (-\frac{(s - \mu_i(x, y))^2}{2\sigma_i(x, y)^2}) \tag{3.30}$$

Parameters $\mu_i(x, y)$ and $\sigma_i(x, y)$ can be estimated by smoothing the image with a Gaussian kernel with standard deviation σ_w within a local window centered at location (x, y) :

$$\mu_i(x, y) = \frac{\int_{\Omega_i} G_{\sigma_w}(\tau_1 - x, \tau_2 - y) \ u(\tau_1, \tau_2) \ d\tau_1 d\tau_2}{\int_{\Omega_i} G_{\sigma_w}(\tau_1 - x, \tau_2 - y) \ d\tau_1 d\tau_2} \tag{3.31}$$

$$\sigma_i^2(x, y) = \frac{\int_{\Omega_i} G_{\sigma_w}(\tau_1 - x, \tau_2 - y) \ (u(\tau_1, \tau_2) - \mu_i(x, y))^2 \ d\tau_1 d\tau_2}{\int_{\Omega_i} G_{\sigma_w}(\tau_1 - x, \tau_2 - y) \ d\tau_1 d\tau_2} \tag{3.32}$$

According to [41], it can be shown that μ_i in Eq. (3.31) is the exact minimizer of:

$$E(\mu_i) = \int_{\Omega_i} \left((\mu_i - u)^2 + \sum_{k=1}^{\infty} \frac{\lambda^k}{k!} \sum_{j_1+j_2=k} (\frac{d^k \mu_i}{dx^{j_1} dy^{j_2}})^2 \right) dxdy \tag{3.33}$$

The local Gaussian density with a fixed standard deviation $\sigma = \sqrt{0.5}$, yields:

$$E(\mu, C) = \sum_i^N \int_{\Omega_i} (\mu_i(x, y) - u(x, y))^2 dxdy + \nu|C| + const \tag{3.34}$$

Therefore, the Bayesian model may be re-written as:

$$E^B(\mu, C) = \sum_i \int_{\Omega_i} \left((\mu_i(x, y) - u(x, y))^2 + \right.$$
$$\left. \sum_{k=1}^{\infty} \frac{\lambda^k}{k!} \sum_{j_1+j_2=k} (\frac{d^k \mu_i}{dx^{j_1} dy^{j_2}})^2 \right) dxdy + \nu|C| + const \tag{3.35}$$

Ultimately, considering the first order approximation of the above equation, i.e. disregarding higher order terms with $k > 1$, the above energy leads exactly to the Mumford-Shah functional in Eq. (2.9):

$$
\begin{aligned}
E^B(\mu, C) &= \sum_i \int_{\Omega_i} \left((\mu_i(x,y) - u(x,y))^2 + \lambda |\nabla \mu_i|^2 \right) \, dxdy + \nu |C| + const. \\
&= E^{MS}(\mu, C)
\end{aligned}
\tag{3.36}
$$

3.4.5 Adding Topology Constraint

Although the automatic handling of topology changes is generally being considered as a great advantage of level set based schemes, such flexibility becomes undesirable in applications where the number of components to be segmented and their topological arrangement are known in advance, as in case of nuclei segmentation with predefined seed points. To address this problem, a topology preserving level set method (TLSM) was proposed in [6] that can be generally applied to all level set based approaches, within a narrow band. TLSM provides an effective strategy to prevent automatic topology changing while maintaining the other advantages of level set over the previously stated parametric approaches, including generation of nonintersecting curves, facilitating the computation by using fixed grid points, and handling sharp corners.

The key idea of TLSM is to monitor the sign of level set function at every iteration and examine a potential sign change to see whether it occurs at a so called "simple point" or at a "non simple point". In accordance with the digital topology context, a simple point is a point whose deletion does not change the topology of the binarized level set function, as shown in Fig.
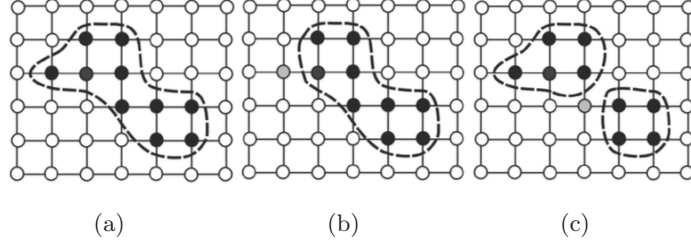
35

| (a) | (b) | (c) |

Figure 3.5: Level set representation on a discrete gird: dark points represent inside the zero level set, where $\phi > 0$. (a) Original level-set. (b) A sign change at a simple point (topology remains unchanged). (c) A sign change at a non-simple point (topology changes).

(3.5). This verification of the candidate point can be obtained through the connected component labeling within the 3×3 neighborhood of the point, using the concepts of Geodesic Neighborhood and Topological Numbers [6, 43] in 2D settings:

I. Geodesic Neighborhood

The geodesic neighborhood of $\mathbf{p} \in V$ with respect to $S \subset V$ of order k is the set $N_n^k(\mathbf{p}, S)$ defined recursively by:

$$N_n^k(\mathbf{p}, S) = \cup \{N_n(\mathbf{q}) \cap N_8^*(\mathbf{p}) \cap S, q \in N_n^{k-1}(\mathbf{p}, S)\},$$

with $N_n^1(\mathbf{p}, S) = N_n^*(\mathbf{p}) \cap S$.

II. Topological Number

The topological numbers of the point $\mathbf{p} \in V$, relative to the set $S \subset V$ are:

$$T_4(\mathbf{p}, S) = \#C_4(N_4^2(\mathbf{p}, S)),$$

$$T_8(\mathbf{p}, S) = \#C_8(N_8^1(\mathbf{p}, S)),$$

where $\#$ denotes the cardinality of a set and $C_n(S)$ represents the set of all n-connected components of $S \subset V$.

In both definitions, $V \subset \mathbb{Z}^2$ is the set of lattice points which represent the binarized image,

$n \in \{4, 8\}$ denotes the connectivity type, and $N_n(\mathbf{p})$ and $N_n^*(\mathbf{p})$ denote the n-neighborhood of the point $\mathbf{p}$, including and excluding $\mathbf{p}$ respectively. It can be shown that a point $\mathbf{p}$ is simple if and only if $T_n(\mathbf{p}, S) = 1$ and $T_{\bar{n}}(\mathbf{p}, \bar{S}) = 1$, where values n and $\bar{n}$ are the connectivity types of foreground and background set of pixels S and $\bar{S}$, and have to be assigned differently. For instance, if n is set to 4, then $\bar{n}$ must be 8. Consequently, the TLSM steps are presented as what follows in algorithm (1).

Even though the topology constraint computations are only being done within a narrow band of the zero level set, calculation of topological numbers at every iteration, decelerate the segmentation process. Consequently, we have used a 511×1 look up table containing every combination of pixels in a 3×3 neighborhood. Although being simple, this significantly improves the performance of segmentation.

In figures (3.6) and (3.6), two histological and fluorescent images are segmented without (3.6.a, 3.7.a) and with (3.6.b, 3.7.b) the topology preserving criteria respectively.

3.4.6 Roundness Energy

In applications where nuclei are priorly known to have a fairly circular structure without elongation , we suggest to add a new roundness energy to the existing energy functional. One way to measure the shape roundness is to calculate the inner product of the gradient vector and the vector connecting each point (x,y) to a specified center point (x_c, y_c). In our case this center point could be easily obtained using Fast Radial Symmetry (FRST) transform. In order to get the desired segmentation as round as possible, we need to maximize: $cos\angle(\vec{r}, \nabla \vec{H}(\phi))$:
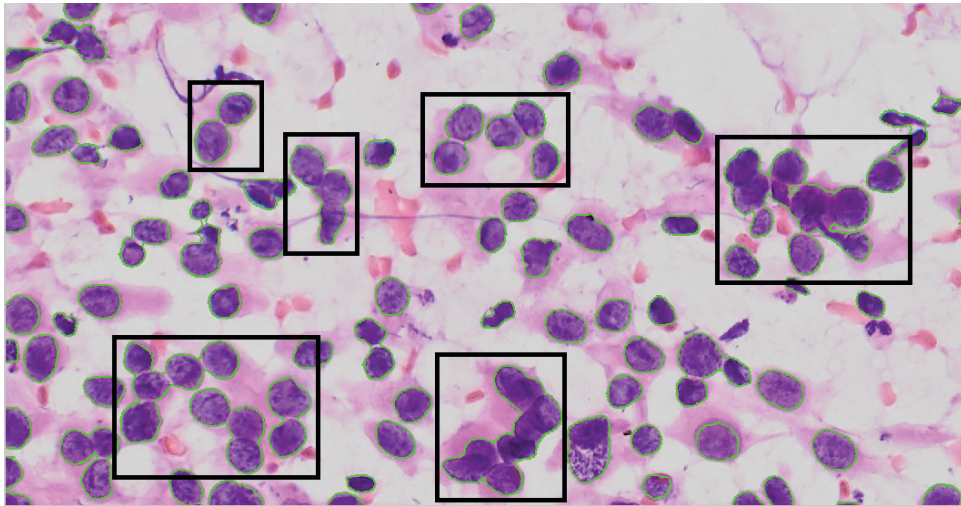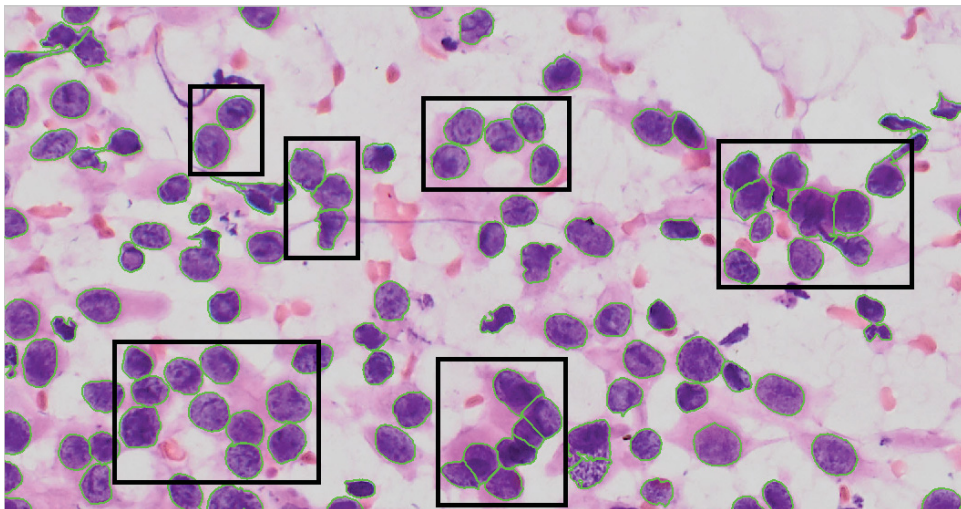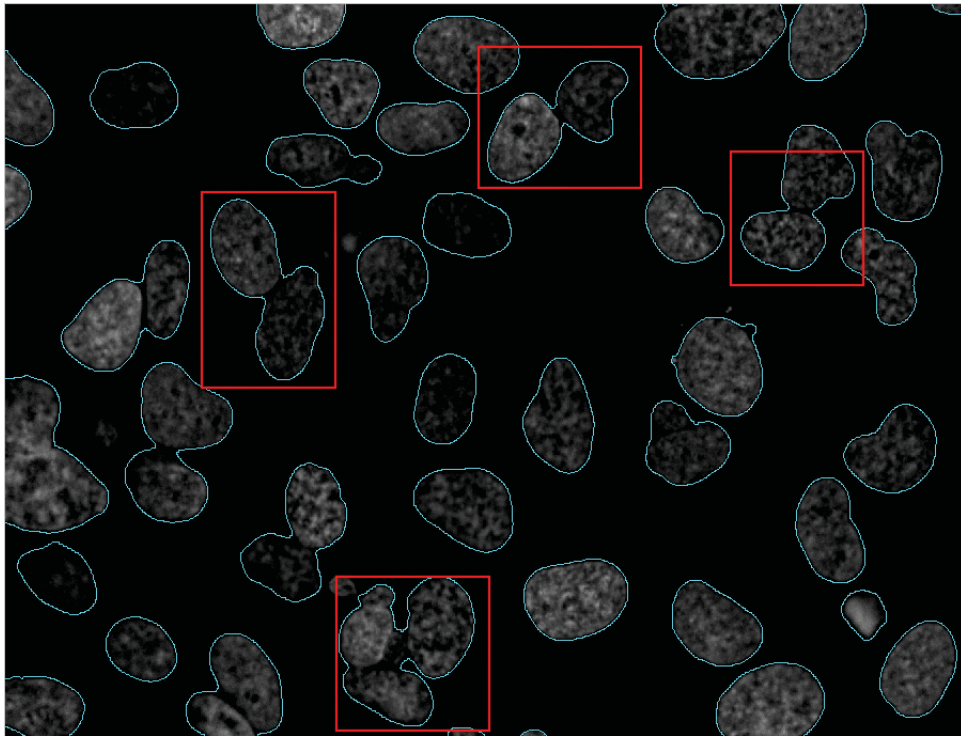
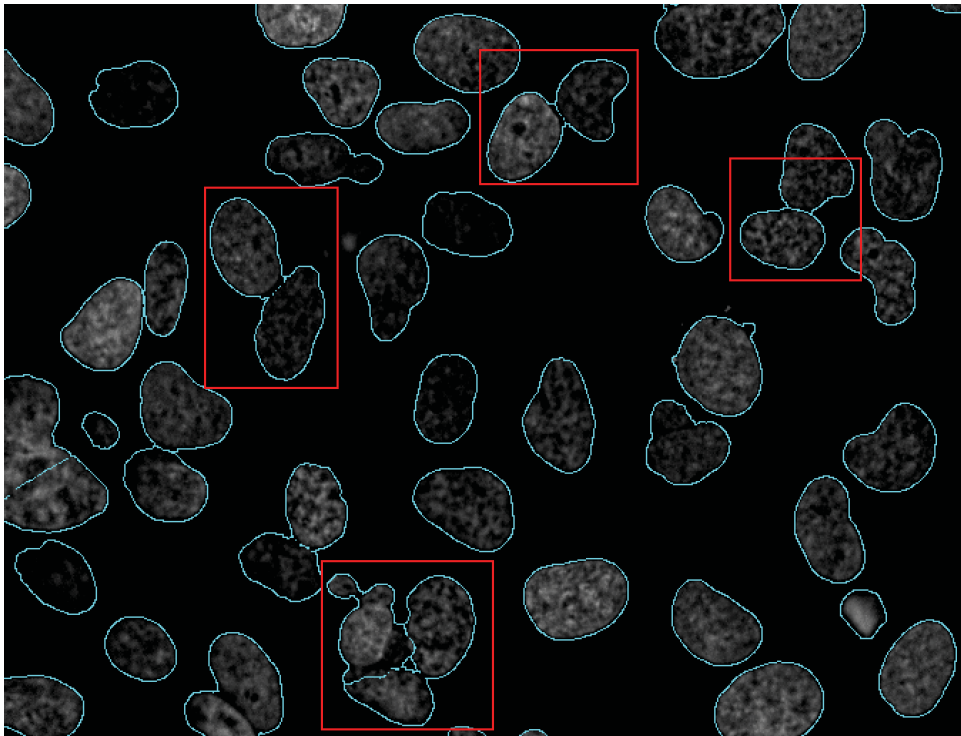Figure 3.6: (a) segmentation of an H&E image without topology preservation (b) segmentation with topology preservation

Figure 3.7: (a) segmentation of a fluorescent image without topology preservation (b) segmentation with topology preservation

39

Algorithm 1 Topology Preserving Level Set

1. Initialize $\phi^0(.)$ to be the signed distance function of the initial contour.

2. Update the level set function within a narrow band $\mathbf{q}_i \in \{\mathbf{p}_i \ |\phi^m(\mathbf{p}_i)| < W_{nb}, \ i = 1, ..., N_{nb}\}$, at iteration $m+1$:

   (a) Compute $\phi^{temp} = \phi^m(\mathbf{q}_i) + \Delta t \ \Delta\phi^m(\mathbf{q}_i)$. If $\text{sign}(\phi^{temp}(\mathbf{q}_i)) = \text{sign}(\phi^m(\mathbf{q}_i))$: set $\phi^{m+1}(\mathbf{q}_i) = \phi^{temp}(\mathbf{q}_i)$, keep $B(\mathbf{q}_i)$ unchanged, and go to step (d) otherwise continue to the next step.

   (b) Compute $T_n(\mathbf{p}, S)$ and $T_{\bar{n}}(\mathbf{p}, \bar{S})$, where S and $\bar{S}$ are the foreground and background pixels such that: $X = \{\mathbf{p}_i; \ B(\mathbf{p}_i) = 1\}$ and $\bar{S} = \{\mathbf{p}_i; \ B(\mathbf{p}_i) = 0\}$. If $T_n(\mathbf{p}, S) = T_{\bar{n}}(\mathbf{p}, \bar{S}) = 1$: set $\phi^{m+1}(\mathbf{y}_i) = \phi^{temp}(\mathbf{y}_i)$, $B(\mathbf{y}_i) = 1 - B(\mathbf{y}_i)$ and go to step (d) otherwise continue to the next step.

   (c) Set $\phi^{m+1}(\mathbf{q}_i) = \epsilon \ . \ sign(\phi^m(\mathbf{q}_i))$ and keep $B(\mathbf{q}_i)$ unchanged.

   (d) If $i \leq N_{nb}$, then set $i = i+1$, otherwise go to step (4).

3. Reinitialize the level set function to the signed distance function of the current curve.

4. Terminate the algorithm if the zero level set has stopped moving, otherwise set $m = m+1$ and go back to step (2).

$$E_R = \iint cos\angle(\vec{r}, \nabla H(\phi)) = \iint\limits_{x,y \in C} \frac{\vec{r} . \nabla \vec{H}(\phi)}{|| \vec{r} || . || \nabla \vec{H}(\phi) ||} dxdy \tag{3.37}$$

$|| \nabla \vec{H}(\phi) || = 1$ and $\nabla \vec{H}(\phi) = \delta(\phi) . \nabla(\phi)$ so,

$$E_R = \iint \frac{\vec{r} . \vec{\nabla}\phi}{|| \vec{r} ||}, \ \delta(\phi) dxdy = \iint \frac{(x - x_C).\phi_x + (y - y_C).\phi_y}{\sqrt{(x - x_C)^2 + (y - y_C)^2}} \delta(\phi) dxdy$$
$$= \iint g(x, y, \phi(x, y), \phi_x(x, y), \phi_y(x, y)) \tag{3.38}$$

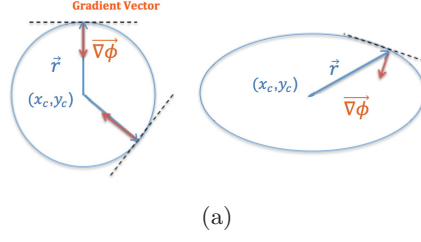Using the Euler Lagrange Equation the gradient descent can be obtained:

(a)

Figure 3.8: Illustration of roundness measurement.

$$\nabla E_R = \frac{\partial g}{\partial \phi} - \frac{\partial}{\partial x}\frac{\partial g}{\partial \phi_x} - \frac{\partial}{\partial y}\frac{\partial g}{\partial \phi_y} = -\frac{1}{\sqrt{(x-x_C)^2 + (y-y_C)^2}}\delta(\phi) \qquad (3.39)$$

$$\frac{\partial g}{\partial \phi_x} = \frac{x-x_C}{\sqrt{(x-x_C)^2+(y-y_C)^2}}\delta(\phi)\,, \qquad \frac{\partial}{\partial x}\frac{\partial g}{\partial \phi_x} = \frac{(y-y_C)^2}{(x-x_C)^2+(y-y_C)^2(3/2)}\delta(\phi) + \frac{(x-x_C).\phi_x}{\sqrt{(x-x_C)^2+(y-y_C)^2}}\delta'(\phi)$$

$$\frac{\partial g}{\partial \phi_y} = \frac{y-y_C}{\sqrt{(x-x_C)^2+(y-y_C)^2}}\delta(\phi), \qquad \frac{\partial}{\partial y}\frac{\partial g}{\partial \phi_y} = \frac{(x-x_C)^2}{(x-x_C)^2+(y-y_C)^2(3/2)}\delta(\phi) + \frac{(y-y_C).\phi_y}{\sqrt{(x-x_C)^2+(y-y_C)^2}}\delta'(\phi)$$

$$\frac{\partial \phi_R}{\partial t} = -\nabla E = \frac{1}{\sqrt{(x-x_C)^2+(y-y_C)^2}}\delta(\phi) \qquad (3.40)$$

$$E = E^{Region} + \beta E^{Roundness} + \nu|C|. \qquad (3.41)$$

Finally, the gradient descent equation with shape roundness prior is determined by:

$$\frac{\partial \phi}{\partial t} = \delta(\phi)\Big(log\,\frac{p_1(u(x,y))}{p_2(u(x,y))} + \beta\frac{1}{\sqrt{(x-x_C)^2+(y-y_C)^2}} + \nu\,div\,\frac{\nabla\phi}{|\nabla\phi|}\Big) \qquad (3.42)$$

3.4.7 The Proposed Method

The overview of the proposed nuclei segmentation pipeline is presented in algorithm2. An important property of the proposed method is that all the computations are required only in a narrow band within the curve. The proposed framework does not add too much computational complexity to the regular level set based narrow band implementation. In fact, at the first stage of the pipeline, computation of GFRS ellipses is of the order $O(Kl)$, where K is the total number of pixels and l is the number of affine transformations (in this thesis $l = 36$). All the other computations are linear with the total number of pixels. To compute the gradient descent of equation (3.23) we have implemented two commonly used finite difference schemes: Forward Time Centered Space (FTCS) and Alternating Directional Implicit (ADI). More details on the numerical approximations of these schemes can be found in [54].

Algorithm 2 Proposed Method
---

1. Convert RGB image to grayscale using color deconvolution method in section 3.1.

2. Calculate GFRS transforms of the image $MAP = \{MAP_1, MAP_2, ..., MAP_l\}$, where l is the total number of affine transformations. If the overall nuclei symmetry in the dataset is circular use the FRST transform to obtain $MAP = \{MAP_1\}$.

3. Apply non-maxima suppression on MAP to find the local maxima of each transform $S = \left\{\{p_{11}, p_{12}, ...\}, \{p_{21}, p_{22}, ...\}, ..., \{p_{l1}, p_{l2}, ...\}\right\}$ and store their associated parameters A_i, B_i, θ_i. If you have used the FRST transform go to step (5).

4. Re-apply non-maxima suppression on S to obtain Initial seed ellipses $S_c = \{p_1, p_2, ..., p_k\}$, $A_c = \{a_1, a_2, ..., a_k\}$, $B_c = \{b_1, b_2, ..., b_k\}$, $\theta_c = \{\theta_1, \theta_2, ..., \theta_k\}$,

5. Initialize the level set $\phi^0(.)$to the signed distance function of initial ellipses obtained from previous step. (Rescale parameters A_c and B_c.)

6. Update the level set function within a narrow band $\mathbf{q}_i \in \{\mathbf{p}_i \ |\phi^m(\mathbf{p}_i)| < W_{nb}, \ i = 1, ..., N_{nb}\}$, at iteration $m + 1$:

   (a) Compute $\phi^{temp} = \phi^m(\mathbf{q}_i) + \Delta t \ \Delta\phi^m(\mathbf{q}_i)$ according to equation 3.23 or 3.42 (If you have used the FRST transform). Use Gaussian approximation or Parzen density estimation. If $\text{sign}(\phi^{temp}(\mathbf{q}_i) = \text{sign}(\phi^m(\mathbf{q}_i)$: set $\phi^{m+1}(\mathbf{q}_i) = \phi^{temp}(\mathbf{q}_i)$, keep $B(\mathbf{q}_i)$ unchanged, and go to step (d) otherwise continue to the next step.

   (b) extract the 3×3 neighboring points of $\mathbf{q}_i$ and use topology look-up table to check if the point is simple or not. if $\mathbf{q}_i$ is simple set $\phi^{m+1}(\mathbf{y}_i) = \phi^{temp}(\mathbf{y}_i)$, $B(\mathbf{y}_i) = 1 - B(\mathbf{y}_i)$ and go to step (d) otherwise continue to the next step.

   (c) Set $\phi^{m+1}(\mathbf{q}_i) = \epsilon \ . \ sign(\phi^m(\mathbf{q}_i))$ and keep $B(\mathbf{q}_i)$ unchanged.

   (d) If $i \leq N_{nb}$, then set $i = i + 1$, otherwise go to step (8).

7. Reinitialize the level set function to the signed distance function of the current curve.

8. Terminate the algorithm if the the zero level set has stopped moving, otherwise set $m = m + 1$ and go back to step (6).

Chapter 4

Experimental Results and Discussions

In this chapter, several examples of cyto-histopathological images are examined to validate the proposed method. Our experiments involve two main types of microscopic images: (I) H&E stained images, (II) Fluorescent images. Since we couldn't find a valid segmentation dataset of H&E stained images, we limited our experiments of H&E images to the qualitative analysis of segmented results.

4.1 Hematoxylin and Eosin (H&E) Stained Images

In figures (4.1 - 4.3) three histopathological sections of benign and malignant specimens are segmented using three different methods: marker controlled watershed on image gradient, thresholding method along with nuclei separation, and the proposed energy-based method with Gaussian statistical model. For all three methods, Hematoxylin and Eosin images are first deconvolved according to [3]. Also the initial markers of watershed method are obtained using the GFRS

algorithm [5]. In figure (4.5) the same methodologies has been applied to the blue channel of the
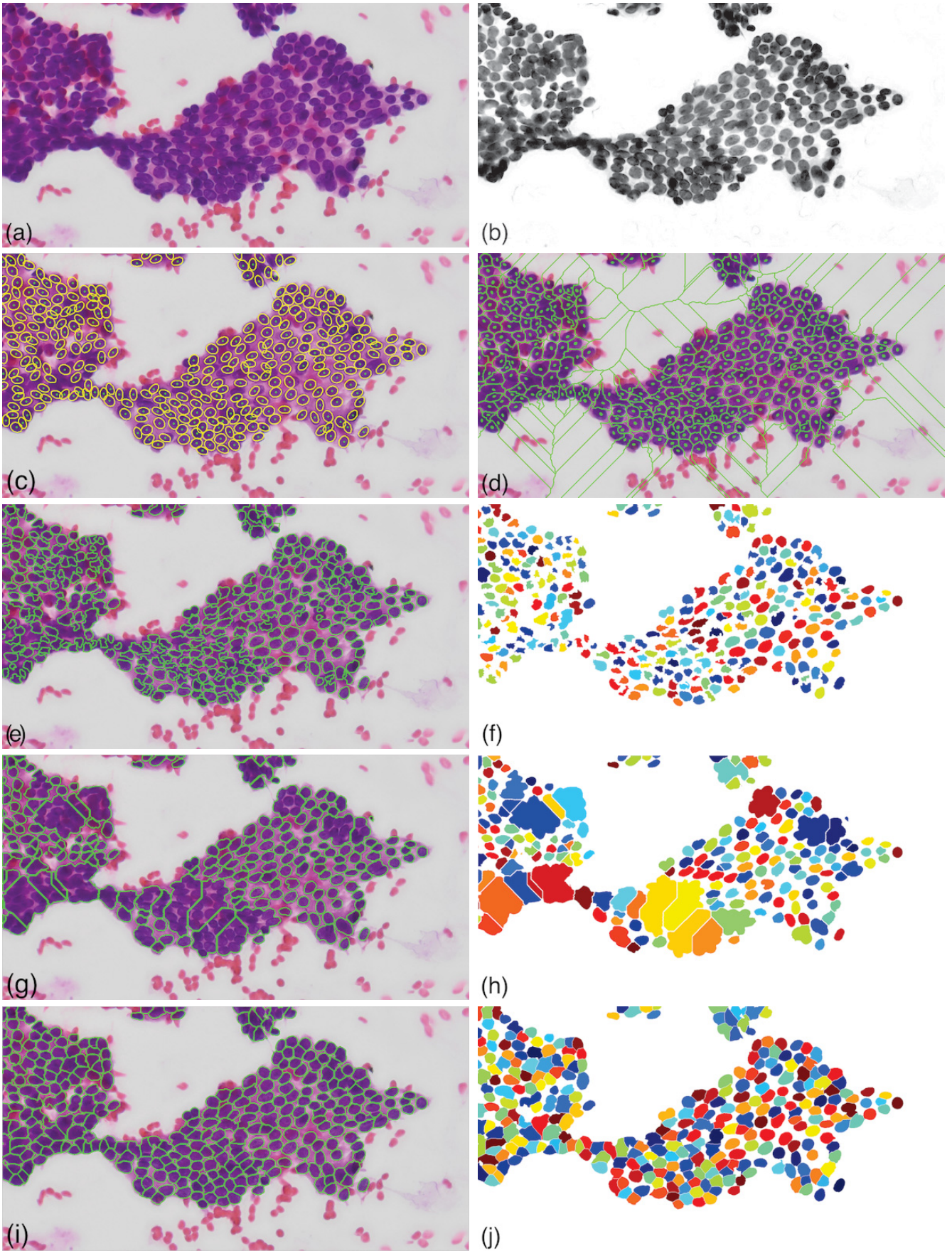input color image.

Figure 4.1: Comparison of different segmentation results on a Benign H&E tissue section. (a) Original Image (of size 1583×828, 40x magnification). (b) Original Image after color deconvolution. (c) Initial ellipses obtained from GFRS. (d) Initial watershed markers based on initial ellipses in (c). (e,f) Watershed (gradient) segmentation of (d). (g,h) Maximum correlation thresholding (MCT) segmentation of (b) and shape-based separation (CellProfiler Automatic strategy, the desired range of cells diameter is set to [10 30]). (i,j) Proposed Method.($a = \{20\}, b = \{0.6, 0.8\} * a, \theta = k\pi/8$, $k = 0, 1, .., 8$)
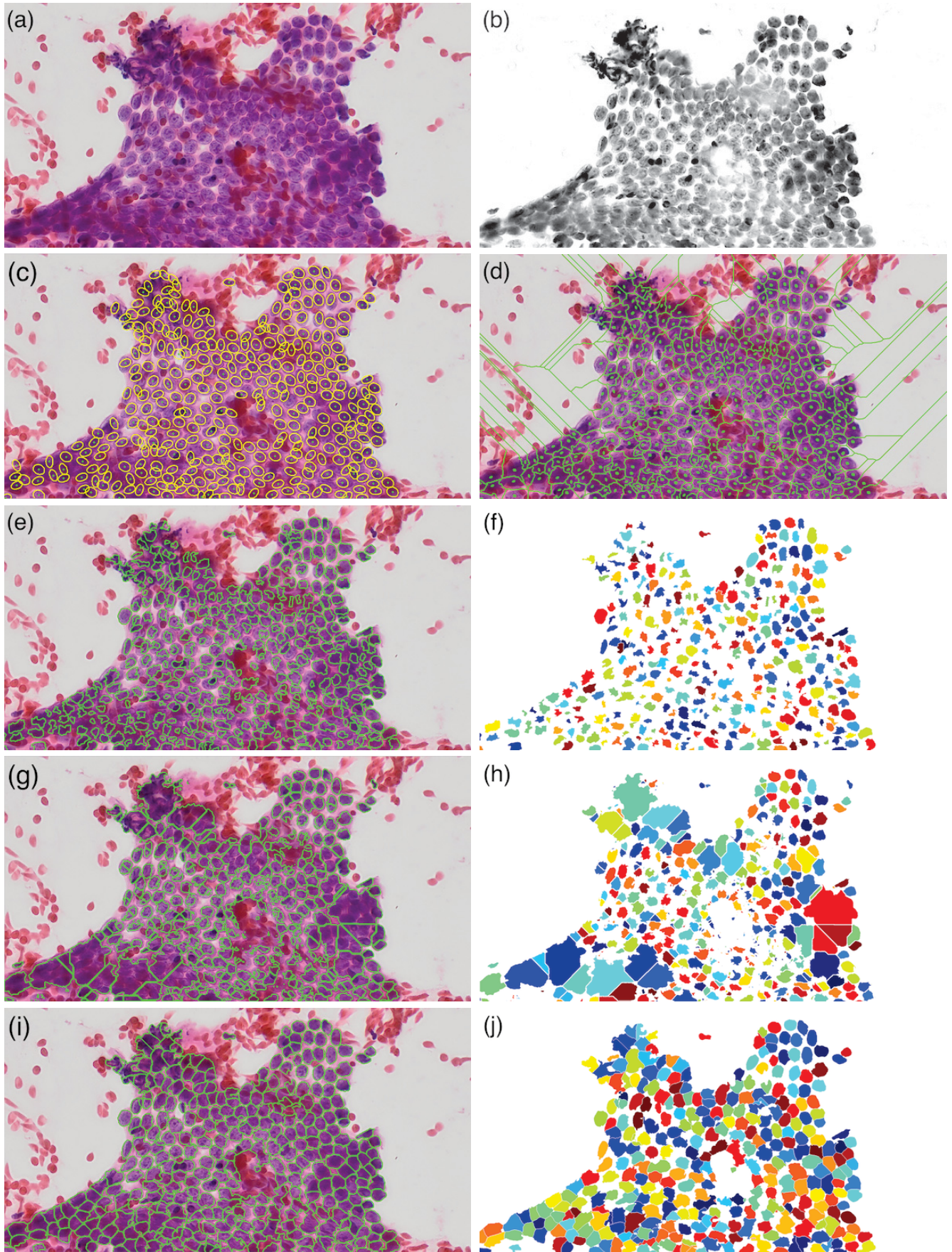
Figure 4.2: Comparison of different segmentation results on a Benign H&E tissue section. (a) Original Image. (of size 1583×828, 40x magnification). (b) Original Image after color deconvolution. (c) Initial ellipses obtained from GFRS. (d) Initial watershed markers based on initial ellipses in (c). (e,f) Watershed segmentation of (d). (g,h) Maximum correlation thresholding (MCT) segmentation of (b) and shape-based separation (CellProfiler Automatic strategy, the desired range of cells diameter is set to [10 30]). (i,j) Proposed Method.($a = \{20\}, b = \{0.6, 0.8\} * a, \theta = k\pi/8$, $k = 0, 1, .., 8$)

Figure 4.3: Comparison of different segmentation results on a Malignant H&E tissue section. (a) Original Image. (of size 1583 × 828, 40x magnification).(b) Original Image after color deconvolution. (c) Initial ellipses obtained from GFRS. (d) Initial watershed markers based on initial ellipses in (c). (e,f) Watershed segmentation of (d). (g,h) Maximum correlation thresholding (MCT) segmentation of (b) and shape-based separation (CellProfiler Automatic strategy, the desired range of cells diameter is set to [10 30]). (i,j) Proposed Method.($a = \{20\}, b = \{0.6, 0.8\} * a, \theta = k\pi/8$, $k = 0, 1, .., 8$)
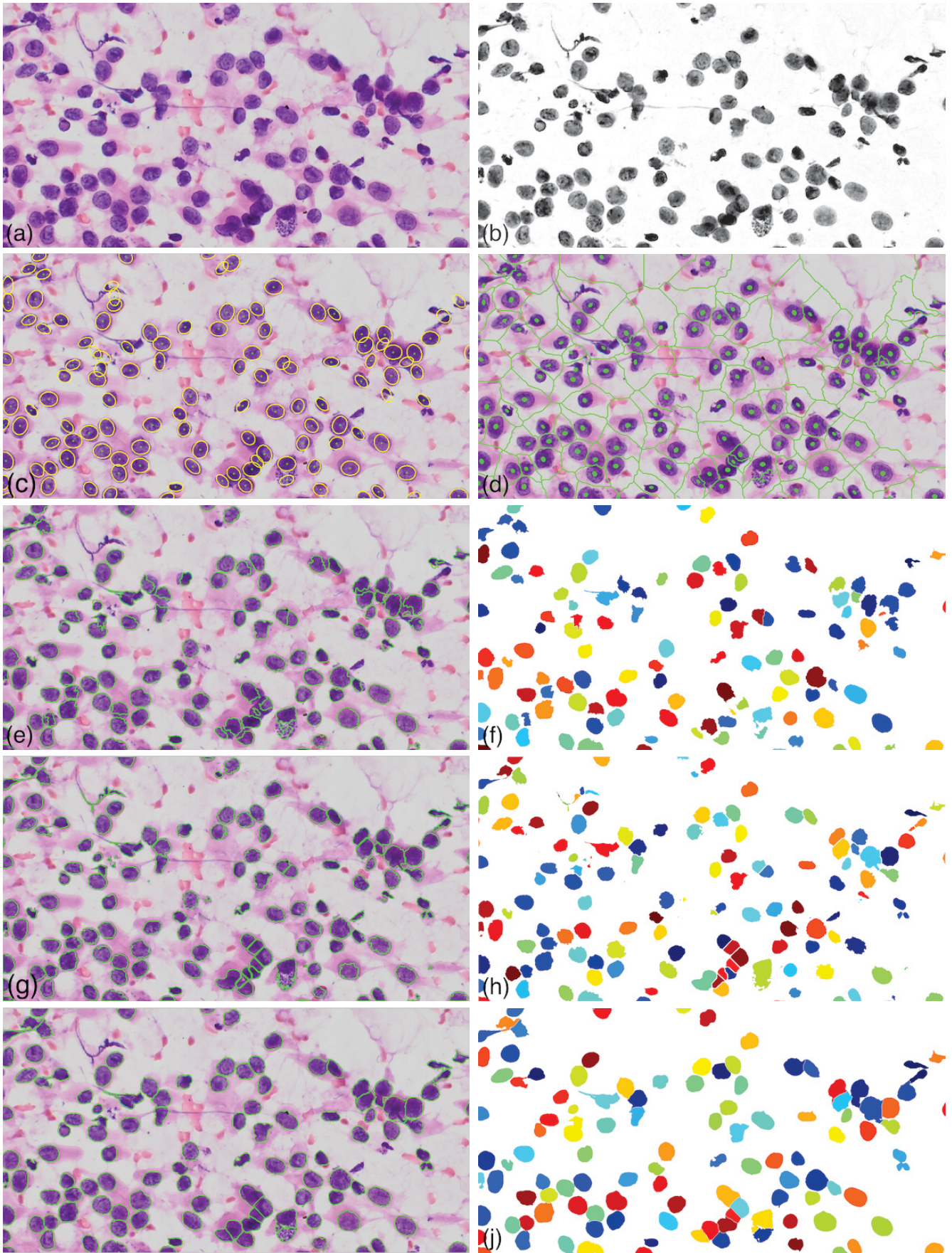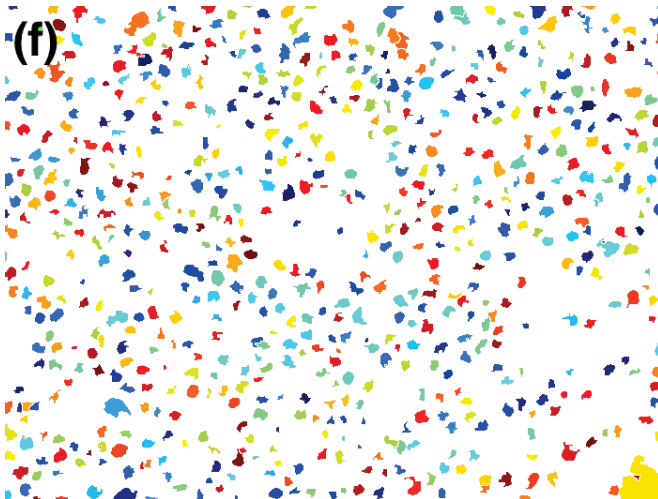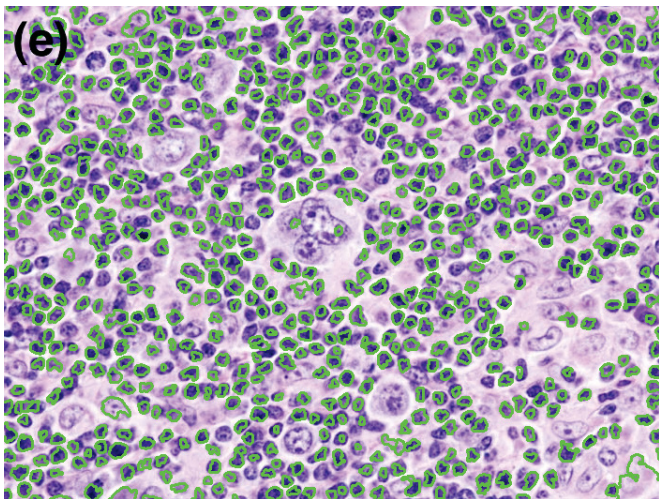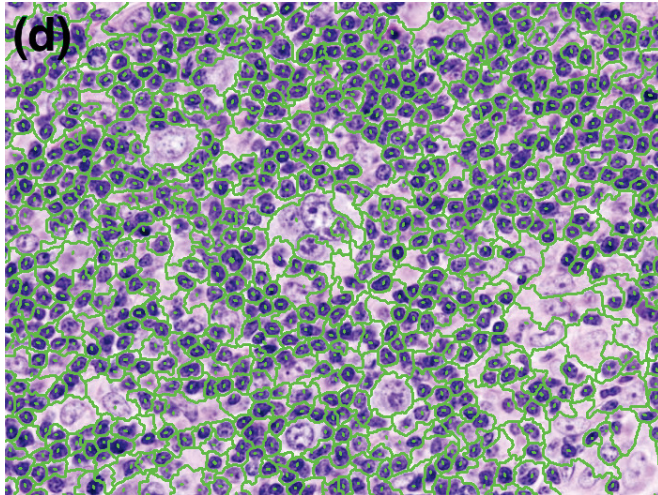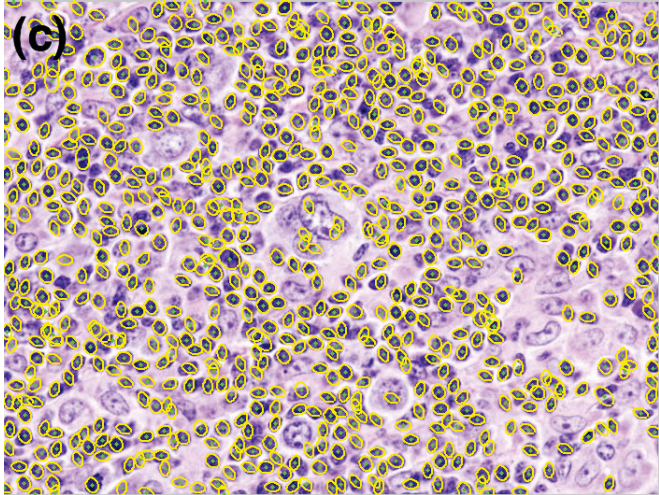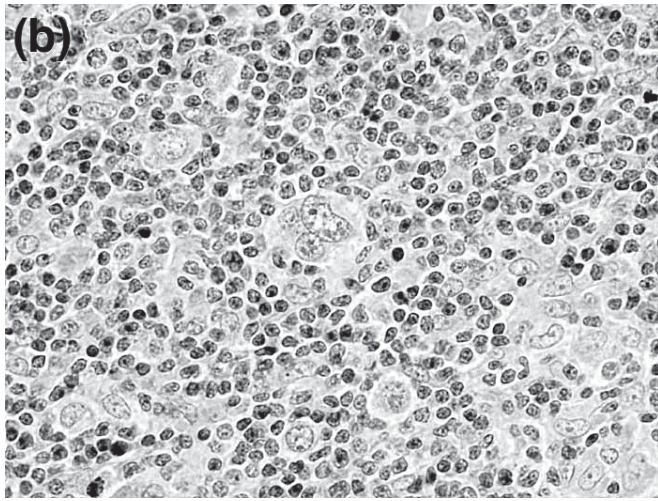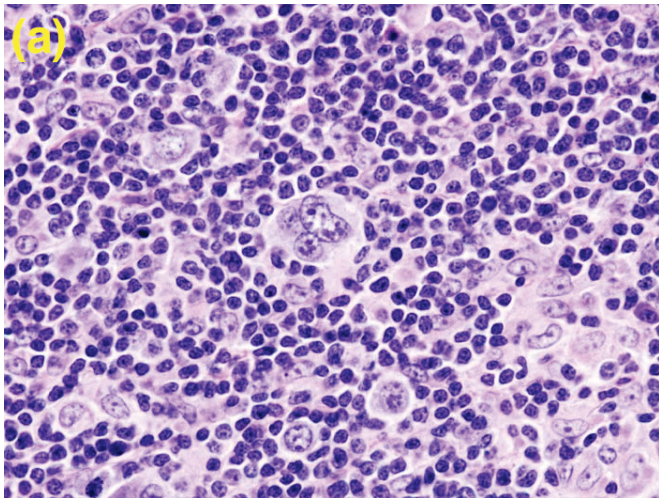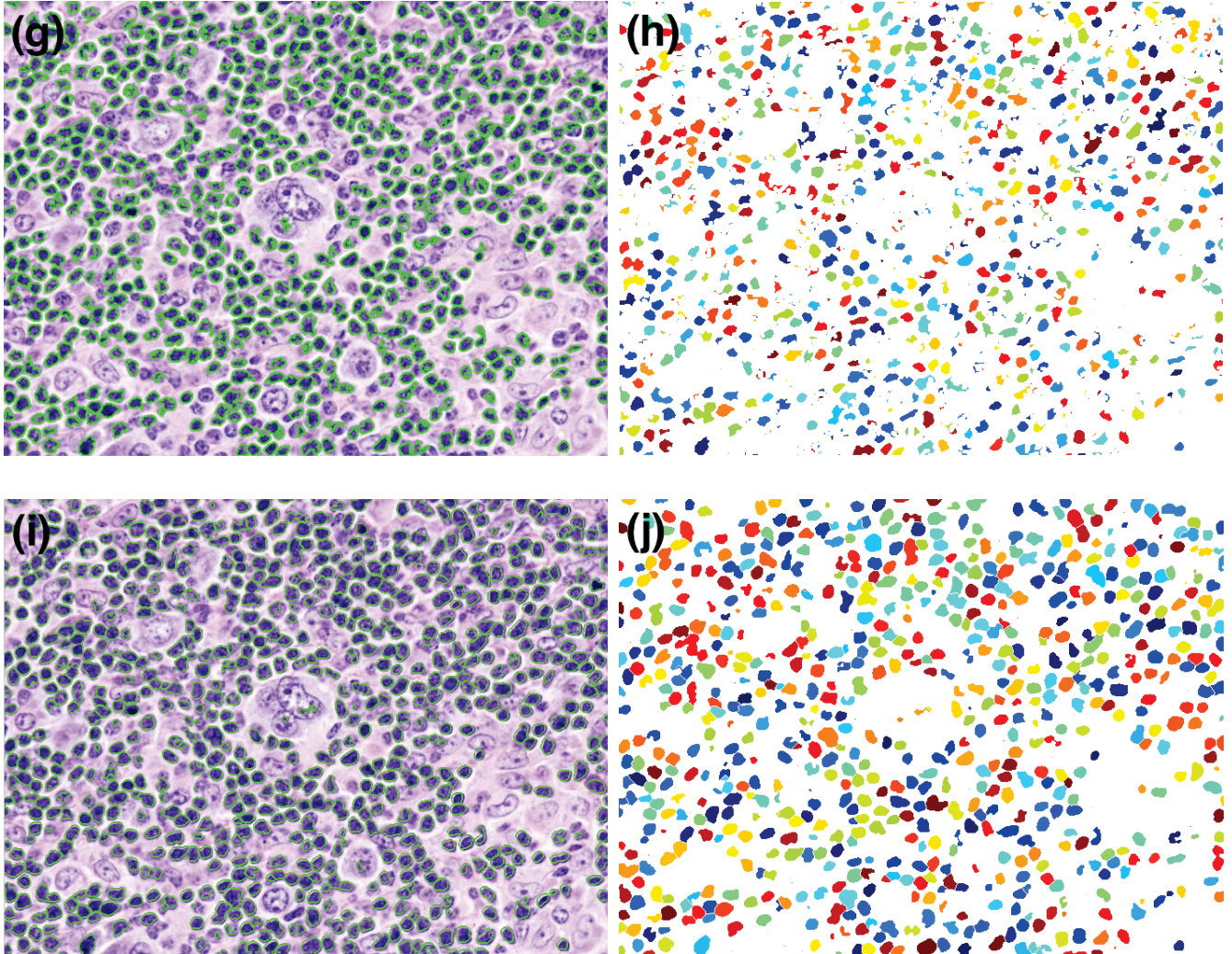
Figure 4.5: Comparison of different segmentation results on a H&E Hodgkin's lymphoma [52]. (a) Original Image. (b) Blue channel of the original image. (c) Initial ellipses obtained from GFRS. (d) Initial watershed markers based on initial ellipses in (c). (e,f) Watershed segmentation of (d). (g,h) Maximum correlation thresholding (MCT) segmentation of (b) and shape-based separation (CellProfiler Automatic strategy, the desired range of cells diameter is set to [5 20]). (i,j) Proposed Method.($a = \{10, 12\}, b = \{0.6, 0.8\} * a, \theta = k\pi/8$, $k = 0, 1, .., 8$)

(a)   (b)   (c)   (d)
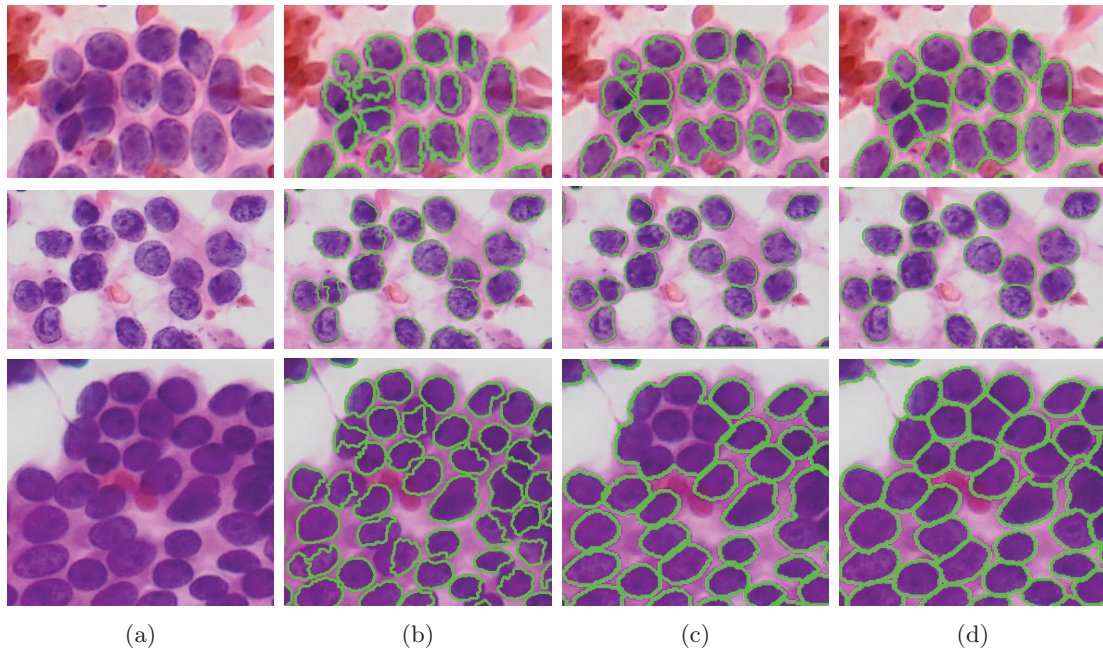
Figure 4.6: Qualitative comparison of different segmentation methods. (a) Original Image (b) Watershed segmentation with GFRS initial markers (c) Maximum correlation thresholding (MCT) segmentation and shape-based separation (CellProfiler Automatic strategy) on the color de-convolved image (d) Proposed Method.

In figures (4.6) and (4.7), several magnified patches of the segmentation results in figures (4.1 - 4.5) are depicted in more details. As it can be seen from the figure, watershed and thresholding methods have failed to segment the entire nuclei area whereas the proposed curve evolution method has been greatly successful in reaching nuclei borders.

| (a) | (b) | (c) | (d) |
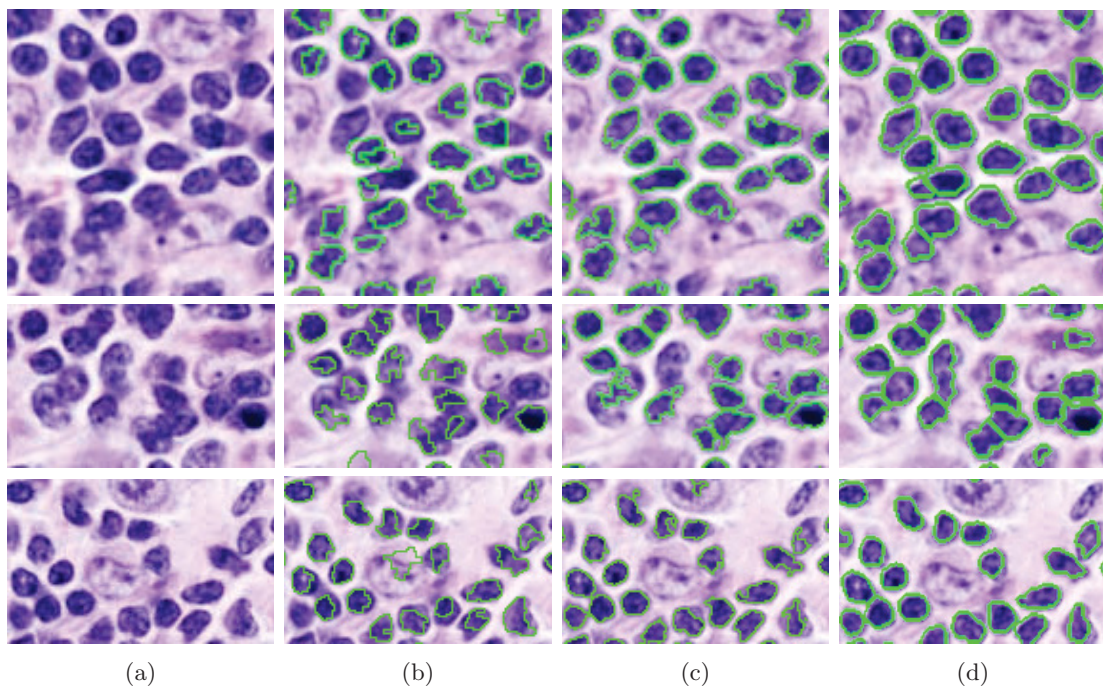
Figure 4.7: Qualitative comparison of different segmentation methods. (a) Original Image (b) Watershed segmentation with GFRS initial markers (c) Maximum correlation thresholding (MCT) segmentation and shape-based separation (CellProfiler Automatic strategy) on the color de-convolved image (d) Proposed Method.
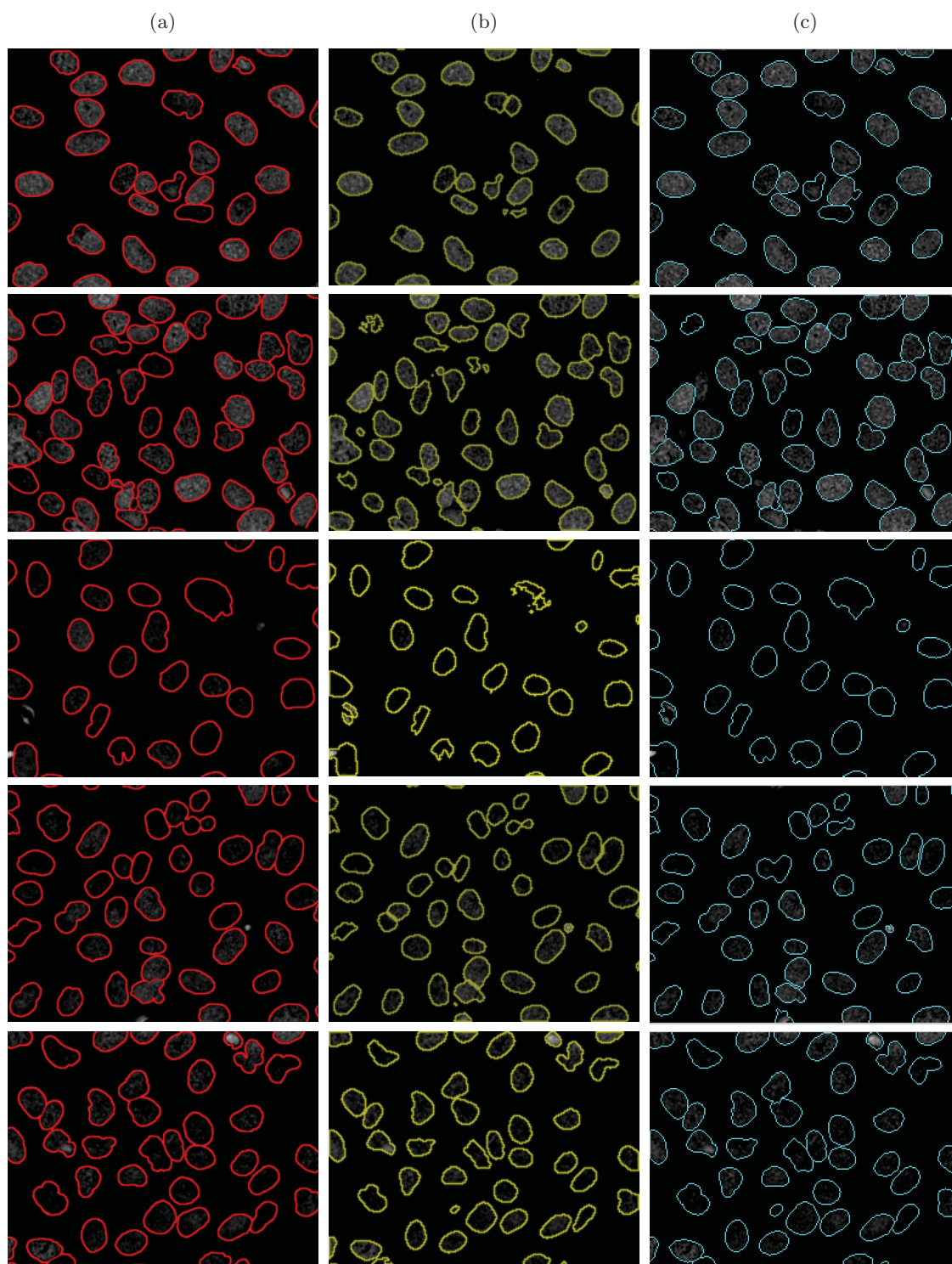
Figure 4.8: Fluorescence microscopy image segmentation. (a) The ground truth segmentation results presented in [2]. (b) The CellProfiler [1] segmentation results using thresholding technique and shape prior for distinguishing clumped objects. (The desired range of cells diameter is set to [80 120]) (c) Segmentation results using the proposed method. ($a = \{50, 60\}, b = \{0.6, 0.8\} * a, \theta = k\pi/8$, $k = 0, 1, .., 8$)

4.2 Fluorescent Stained Microscopy Images

To validate our new method, we have also tested our proposed method on a set of 47 fluorescent microscopy images (U2OS cells) proposed in [2]. In all experiments, fixed parameters e.g. major and minor axes (a and b) and smoothness parameter (ν) for all the images have been used. Also, since this dataset contains small nuclei patches on the boundary with small GFRS responses, a simple mean thresholding and nonlinear diffusion are added to the segmentation pipeline. In Fig. (4.8) we have compared the proposed method with the CellProfiler previously mentioned nuclei segmentation unit: Maximum correlation thresholding (MCT) segmentation combined with shape-based separation (CellProfiler Automatic strategy).

4.3 Robustness of the overlapping boundaries and smoothness parameter

For the sake of separating touching nuclei, conventional shape-based approaches usually take the advantage of points of high concavity. In our proposed method however nuclei boundaries automatically tend to occur at points of high curvature by minimizing the total curvature and therefore by setting higher values of smoothness parameter ν. To get accurate and smooth boundaries within the overlapping regions, in first few iterations we set the smoothness parameter to lower values in order for the curve to reach closer to nuclei boundaries, then we set the smoothness parameter to higher values. This will prevent formation of jagged edges in overlapping regions. The effect of smoothness parameter on overlapping edges has been illustrated in figures (4.9.c) and (4.9.d). The smoothness parameter of figure (4.9.d) is chosen twice that of figure (4.9.c).
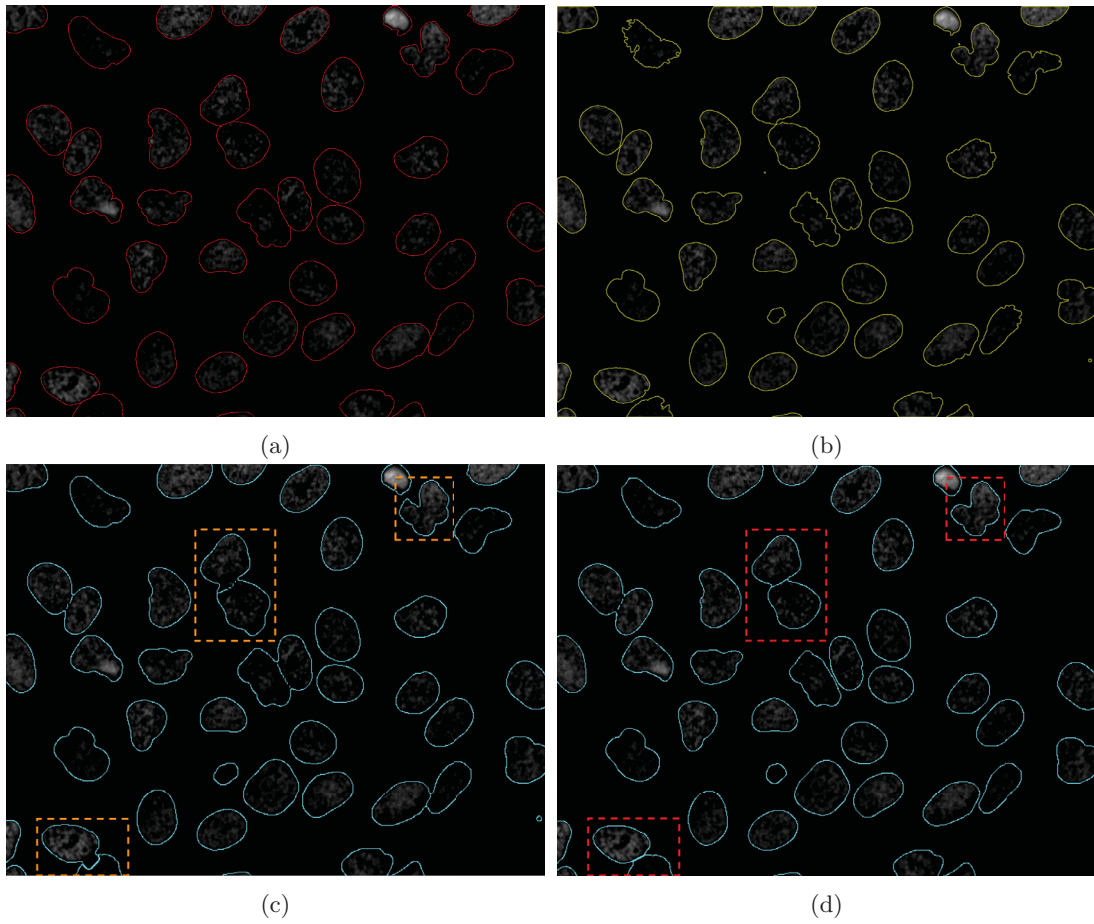
Figure 4.9: Effect of smoothness parameter (a) Ground truth (b) Cell profiler result (c) Proposed method with $\nu = \nu_1$, (d) Proposed method with $\nu = \nu_2, \nu_2 = 2\nu_1$

4.4 Segmentation Evaluation Metrics

Considering the segmentation as a form of data clustering problem, we can use the similarity measurements commonly used for evaluating the clustering results. We have used the Rand and Jaccard indexes used in [2]. Let S and R be the segmented and reference images respectively. For each pair of pixels p_i and p_j, , $i, j = 1, ..., n$, $i \neq j$, where n is the total number of pixels in R and S, there are four possible situations:

True Positive (TP) : $R_i = R_j$, $S_i = S_j$

False Positive (FP) : $R_i \neq R_j$, $S_i = S_j$

False Negative (FN) : $R_i = R_j$, $S_i \neq S_j$

True Negative (TN) : $R_i \neq R_j$, $S_i \neq S_j$

Rand index (RI) measures the percentage of the pairs of pixels where two clusters concur:

$$RI(R, S) = \frac{TP + TN}{TP + FP + FN + TN} \tag{4.1}$$

Similarly, Jaccard index is defined as:

$$JI(R, S) = \frac{TP + TN}{FP + FN + TN} \tag{4.2}$$

In addition to Rand and Jaccard indexes, we also count the number of split, merged, added and missing nuclei in accordance with the metrics presented in [2].

As illustrated in table (1), the proposed method yields in relatively high Rand and Jaccard indices (with the highest Jaccard index). Also, the average number of split, merged and missing nuclei are the minimum.

56

Algorithm	Rand Index	Jaccard Index	Split	Merged	Added	Missing
Expert Manual	95 %	2.4	1.6	1.0	0.8	2.2
RC Threshold	92 %	2.2	1.1	2.4	0.3	5.5
Ostu Threshold	92 %	2.2	1.1	2.4	0.3	5.6
Mean Threshold	96 %	2.2	1.3	3.4	0.9	3.6
Watershed (direct)	91 %	1.9	13.8	1.2	2.0	3.0
Watershed (gradient)	90 %	1.8	7.7	2.0	2.0	2.9
Active Masks	87 %	2.1	10.5	2.1	0.4	10.8
Merging Algorithm	96 %	2.2	1.8	2.1	1.0	3.3
Proposed Method	**95 %**	**2.5**	**0.5**	**0.79**	**0.57**	**0.19**

Table 1: Comparison of different segmentation algorithms in [48–51] according to the results in [2]. (Dataset: U2OS, pixel size: 1349×1030, Nr. Cells: 1831, Min Nr. Cells: 24, Max Nr. Cells: 63)

Chapter 5

Conclusion and Future work

In this thesis, we have addressed the two main problems of active contours for segmenting cytohistological imageries. The main drawback of active contours is the problem of getting stuck in local minima. We have resolved this issue by locating the initial curves as close as possible to the desired objects by utilizing their radial or elliptical symmetric features. Furthermore, we have implicitly combined both boundary and region information through the use of a gradient-based transform (FRST or GFRS) and a region-based active contour. The second issue is that active contour method itself is not capable of separating severely overlapped cells and a separation method (e.g. concavity detection, distance transform, ...) is needed at the ultimate stage. By considering the topology criteria, initial curves no longer merge to each other and no more separation is required. Finally, a new roundness energy is introduced for applications where nuclei are priorly known to have a fairly circular structure without elongation. Experiments in chapter 4 revealed that the statistical model (i.e. Gaussian or Parzen approximation) is much stronger than watershed and thresholding in presence of intensity variation. In other words, watershed and thresholding methods failed to segment the entire nuclei area in regions with significant intensity variations and produced incomplete edges.

As a future work, since the intensity of attached nuclei varies rapidly across the overlapping boundaries, we would suggest to incorporate boundary energy with the existing region-based model. This improvement is expected to generate better results specially at the boundaries of the overlapping regions. Additionally, it is more reasonable to use a image-specific color deconvolution technique rather than a fixed normalized optical density matrix for hematoxylin and eosin stain deconvolution.

Bibliography

[1] A. E. Carpenter, T. R. Jones, M. R. Lamprecht, C. Clarke, I. H. Kang, O. Friman, D. A. Guertin, J. H. Chang, R. A. Lindquist, J. Moffat, *et al.*, "Cellprofiler: image analysis software for identifying and quantifying cell phenotypes," *Genome biology*, vol. 7, no. 10, p. R100, 2006.

[2] L. Coelho, A. Shariff, and R. Murphy, "Nuclear segmentation in microscope cell images: A hand-segmented dataset and comparison of algorithms," in *Biomedical Imaging: From Nano to Macro, 2009. ISBI '09. IEEE International Symposium on*, pp. 518–521, June 2009.

[3] A. C. Ruifrok and D. A. Johnston, "Quantification of histochemical staining by color deconvolution.," *Analytical and quantitative cytology and histology/the International Academy of Cytology [and] American Society of Cytology*, vol. 23, no. 4, pp. 291–299, 2001.

[4] G. Loy and A. Zelinsky, "Fast radial symmetry for detecting points of interest," *IEEE Trans. Pattern Anal. Mach. Intell.*, vol. 25, pp. 959–973, Aug. 2003.

[5] J. Ni, M. Singh, and C. Bahlmann, "Fast radial symmetry detection under affine transformations," in *Computer Vision and Pattern Recognition (CVPR), 2012 IEEE Conference on*, pp. 932–939, June 2012.

[6] X. Han, C. Xu, and J. L. Prince, "A topology preserving level set method for geometric

deformable models," *Pattern Analysis and Machine Intelligence, IEEE Transactions on*, vol. 25, no. 6, pp. 755–768, 2003.

[7] H. Irshad, A. Veillard, L. Roux, and D. Racoceanu, "Methods for nuclei detection, segmentation, and classification in digital histopathology: A review-current status and future potential," *Biomedical Engineering, IEEE Reviews in*, vol. 7, pp. 97–114, 2014.

[8] M. N. Gurcan, T. Pan, H. Shimada, and J. Saltz, "Image analysis for neuroblastoma classification: Segmentation of cell nuclei," in *Engineering in Medicine and Biology Society, 2006. EMBS'06. 28th Annual International Conference of the IEEE*, pp. 4844–4847, IEEE, 2006.

[9] S. D. Cataldo, E. Ficarra, A. Acquaviva, and E. Macii, "Automated segmentation of tissue images for computerized {IHC} analysis," *Computer Methods and Programs in Biomedicine*, vol. 100, no. 1, pp. 1 – 15, 2010.

[10] C. Wählby, I.-M. Sintorn, F. Erlandsson, G. Borgefors, and E. Bengtsson, "Combining intensity, edge and shape information for 2D and 3D segmentation of cell nuclei in tissue sections," *Journal of Microscopy*, vol. 215, no. 1, pp. 67–76, 2004.

[11] R. A. Russell, N. M. Adams, D. A. Stephens, E. Batty, K. Jensen, and P. S. Freemont, "Segmentation of fluorescence microscopy images for quantitative analysis of cell nuclear architecture," *Biophysical journal*, vol. 96, no. 8, pp. 3379–3389, 2009.

[12] S. Di Cataldo, E. Ficarra, A. Acquaviva, and E. Macii, "Automated segmentation of tissue images for computerized IHC analysis," *Computer methods and programs in biomedicine*, vol. 100, no. 1, pp. 1–15, 2010.

[13] C. Jung, C. Kim, S. W. Chae, and S. Oh, "Unsupervised segmentation of overlapped nuclei using bayesian classification," *Biomedical Engineering, IEEE Transactions on*, vol. 57, no. 12, pp. 2825–2832, 2010.

[14] E. Cosatto, M. Miller, H. Graf, and J. Meyer, "Grading nuclear pleomorphism on histological micrographs," in *Pattern Recognition, 2008. ICPR 2008. 19th International Conference on*, pp. 1–4, Dec 2008.

[15] Y. Al-Kofahi, W. Lassoued, W. Lee, and B. Roysam, "Improved automatic detection and segmentation of cell nuclei in histopathology images," *Biomedical Engineering, IEEE Transactions on*, vol. 57, pp. 841–852, April 2010.

[16] P. Soille, *Morphological image analysis: principles and applications*. Springer Science & Business Media, 2013.

[17] O. Dzyubachyk, W. van Cappellen, J. Essers, W. Niessen, and E. Meijering, "Advanced level-set-based cell tracking in time-lapse fluorescence microscopy," *Medical Imaging, IEEE Transactions on*, vol. 29, pp. 852–867, March 2010.

[18] F. Cloppet and A. Boucher, "Segmentation of complex nucleus configurations in biological images," *Pattern Recognition Letters*, vol. 31, no. 8, pp. 755–761, 2010.

[19] Q. Wen, H. Chang, and B. Parvin, "A delaunay triangulation approach for segmenting clumps of nuclei," in *Biomedical Imaging: From Nano to Macro, 2009. ISBI '09. IEEE International Symposium on*, pp. 9–12, June 2009.

[20] C. Jung and C. Kim, "Segmenting clustered nuclei using h-minima transform-based marker extraction and contour parameterization," *Biomedical Engineering, IEEE Transactions on*, vol. 57, pp. 2600–2604, Oct 2010.

[21] J. Cheng and J. Rajapakse, "Segmentation of clustered nuclei with shape markers and marking function," *Biomedical Engineering, IEEE Transactions on*, vol. 56, pp. 741–748, March 2009.

[22] Y. M. George, B. M. Bagoury, H. H. Zayed, and M. I. Roushdy, "Automated cell nuclei segmentation for breast fine needle aspiration cytology," *Signal Processing*, vol. 93, no. 10, pp. 2804–2816, 2013.

[23] P. Quelhas, M. Marcuzzo, A. M. Mendonça, and A. Campilho, "Cell nuclei and cytoplasm joint segmentation using the sliding band filter," *Medical Imaging, IEEE Transactions on*, vol. 29, no. 8, pp. 1463–1473, 2010.

[24] A. Rosenfeld and J. L. Pfaltz, "Sequential operations in digital picture processing," *J. ACM*, vol. 13, pp. 471–494, Oct. 1966.

[25] R. O. Duda and P. E. Hart, "Use of the hough transformation to detect lines and curves in pictures," *Commun. ACM*, vol. 15, pp. 11–15, Jan. 1972.

[26] F. Tek, A. Dempster, and I. Kale, "Blood cell segmentation using minimum area watershed and circle radon transformations," in *Mathematical Morphology: 40 Years On* (C. Ronse, L. Najman, and E. Decencire, eds.), vol. 30 of *Computational Imaging and Vision*, pp. 441–454, Springer Netherlands, 2005.

[27] D. Ballard, "Generalizing the hough transform to detect arbitrary shapes," *Pattern Recognition*, vol. 13, no. 2, pp. 111 – 122, 1981.

[28] Q. Yang and B. Parvin, "Harmonic cut and regularized centroid transform for localization of subcellular structures," *Biomedical Engineering, IEEE Transactions on*, vol. 50, pp. 469–475, April 2003.

[29] H. Kobatake and S. Hashimoto, "Convergence index filter for vector fields," *Image Processing, IEEE Transactions on*, vol. 8, no. 8, pp. 1029–1038, 1999.

[30] J. Wei, Y. Hagihara, and H. Kobatake, "Detection of cancerous tumors on chest x-ray

images-candidate detection filter and its evaluation," in *Image Processing, 1999. ICIP 99. Proceedings. 1999 International Conference on*, vol. 3, pp. 397–401, IEEE, 1999.

[31] C. Pereira, H. Fernandes, A. Mendonça, and A. Campilho, "Detection of lung nodule candidates in chest radiographs," *Pattern Recognition and Image Analysis*, pp. 170–177, 2007.

[32] T. Esteves, P. Quelhas, A. M. Mendonça, and A. Campilho, "Gradient convergence filters and a phase congruency approach for in vivo cell nuclei detection," *Machine Vision and Applications*, vol. 23, no. 4, pp. 623–638, 2012.

[33] M. Kass, A. Witkin, and D. Terzopoulos, "Snakes: Active contour models," *International journal of computer vision*, vol. 1, no. 4, pp. 321–331, 1988.

[34] V. Caselles, R. Kimmel, and G. Sapiro, "Geodesic active contours," *International journal of computer vision*, vol. 22, no. 1, pp. 61–79, 1997.

[35] D. Mumford and J. Shah, "Optimal approximations by piecewise smooth functions and associated variational problems," *Communications on pure and applied mathematics*, vol. 42, no. 5, pp. 577–685, 1989.

[36] S. Gao, "A new image segmentation and smoothing method based on the mumford-shah variational model," *Master of Computer Science Thesis, Concordia University*, 2003.

[37] S. Osher and J. A. Sethian, "Fronts propagating with curvature-dependent speed: algorithms based on hamilton-jacobi formulations," *Journal of computational physics*, vol. 79, no. 1, pp. 12–49, 1988.

[38] T. E. Chan, L. Vese, *et al.*, "A level set algorithm for minimizing the mumford-shah functional in image processing," in *Variational and Level Set Methods in Computer Vision, 2001. Proceedings. IEEE Workshop on*, pp. 161–168, IEEE, 2001.

[39] T. F. Chan, L. Vese, *et al.*, "Active contours without edges," *Image processing, IEEE transactions on*, vol. 10, no. 2, pp. 266–277, 2001.

[40] D. Cremers, M. Rousson, and R. Deriche, "A review of statistical approaches to level set segmentation: integrating color, texture, motion and shape," *International journal of computer vision*, vol. 72, no. 2, pp. 195–215, 2007.

[41] T. Brox and D. Cremers, "On the statistical interpretation of the piecewise smooth mumford-shah functional," in *Scale Space and Variational Methods in Computer Vision* (F. Sgallari, A. Murli, and N. Paragios, eds.), vol. 4485 of *Lecture Notes in Computer Science*, pp. 203–213, Springer Berlin Heidelberg, 2007.

[42] T. Brox, M. Rousson, R. Deriche, and J. Weickert, "Colour, texture, and motion in level set based segmentation and tracking," *Image and Vision Computing*, vol. 28, no. 3, pp. 376 – 390, 2010.

[43] G. Bertrand, "Simple points, topological numbers and geodesic neighborhoods in cubic grids," *Pattern Recognition Letters*, vol. 15, no. 10, pp. 1003 – 1011, 1994.

[44] O. Schmitt and M. Hasse, "Radial symmetries based decomposition of cell clusters in binary and gray level images," *Pattern Recognition*, vol. 41, no. 6, pp. 1905–1923, 2008.

[45] F. Meyer, "Topographic distance and watershed lines," *Signal processing*, vol. 38, no. 1, pp. 113–125, 1994.

[46] J. B. Roerdink and A. Meijster, "The watershed transform: Definitions, algorithms and parallelization strategies," *Fundamenta Informaticae*, vol. 41, pp. 187–228, Apr. 2000.

[47] A. Hafiane, F. Bunyak, and K. Palaniappan, "Clustering initiated multiphase active contours and robust separation of nuclei groups for tissue segmentation," in *Pattern Recognition, 2008. ICPR 2008. 19th International Conference on*, pp. 1–4, Dec 2008.

[48] T. Ridler and S. Calvard, "Picture thresholding using an iterative selection method," *Systems, Man and Cybernetics, IEEE Transactions on*, vol. 8, pp. 630–632, Aug 1978.

[49] N. Otsu, "A threshold selection method from gray-level histograms," *Automatica*, vol. 11, no. 285-296, pp. 23–27, 1975.

[50] G. Srinivasa, M. Fickus, M. Gonzalez-Rivero, S. Hsieh, Y. Guo, A. Linstedt, and J. Kovacevic, "Active mask segmentation for the cell-volume computation and golgi-body segmentation of hela cell images," in *Biomedical Imaging: From Nano to Macro, 2008. ISBI 2008. 5th IEEE International Symposium on*, pp. 348–351, May 2008.

[51] G. Lin, U. Adiga, K. Olson, J. F. Guzowski, C. A. Barnes, and B. Roysam, "A hybrid 3d watershed algorithm incorporating gradient cues and object models for automatic segmentation of nuclei in confocal image stacks," *Cytometry Part A*, vol. 56, no. 1, pp. 23–36, 2003.

[52] Wikipedia, the free encyclopedia, "File:hodgkin lymphoma (3) mixed cellularity type.jpg," Accessed: Feb. 2016.

[53] J. Weickert, B. T. H. Romeny, and M. A. Viergever, "Efficient and reliable schemes for nonlinear diffusion filtering," *Image Processing, IEEE Transactions on*, vol. 7, no. 3, pp. 398–410, 1998.

[54] S. Gao and T. D. Bui, "A multistage image segmentation and denoising method–based on the mumford and shah variational approach," in *Image Analysis and Recognition*, pp. 82–89, Springer, 2004.

[55] H. Kong, M. Gurcan, and K. Belkacem-Boussaid, "Partitioning histopathological images: an integrated framework for supervised color-texture segmentation and cell splitting," *Medical Imaging, IEEE Transactions on*, vol. 30, no. 9, pp. 1661–1677, 2011.